Computer Modeling in Engineering & Sciences

Tech Science Press

https://doi.org/10.32604/cmes.2026.087205

ARTICLE

Prediction of Full-Field Mechanical Response of Membrane Materials under Biaxial Tension Using a CAE-ET Model

Jinpeng Zuo[1,2], **Yingying Zhang**[1,2,*], **Shuhuan Fei**[1,2], **Junhao Xu**[1,2] **and Yushuai Zhao**[1,2]

[1]State Key Laboratory of Intelligent Construction and Healthy Operation and Maintenance of Deep Underground Engineering, China University of Mining and Technology, Xuzhou, China

[2]Jiangsu Key Laboratory of Disaster Impact and Intelligent Prevention in Civil Engineering, China University of Mining and Technology, Xuzhou, China

*Corresponding Author: Yingying Zhang. Email: zhangyingying_cumt@163.com

Received: 11 June 2026; Accepted: 04 September 2026; Published: 21 October 2026

ABSTRACT: The full-field mechanical response of membrane materials under biaxial tension is an important basis for characterizing material mechanical behavior and developing constitutive models. However, conventional finite element analysis requires separate calculations for different constitutive models and loading conditions, making it difficult to efficiently obtain full-field stress, strain, and displacement responses. This study proposes a finite element surrogate model integrating a convolutional autoencoder (CAE) and extremely randomized trees (ET) to rapidly predict full-field mechanical responses of membrane materials under biaxial tension. Based on orthotropic and hyperelastic constitutive models, finite element datasets covering various biaxial load ratios were constructed for training and evaluation, and the finite element model was validated using digital image correlation (DIC) experiments. Under identical sample conditions, ET, deep neural network (DNN), and long short-term memory network (LSTM) were compared for regression of CAE latent codes; ET showed higher accuracy and stability. ET was therefore adopted as the nonlinear fitting layer, and the proposed CAE-ET model was verified using cruciform membrane specimens with the two constitutive descriptions. Results show that CAE-ET accurately predicts the full-field responses of both membrane materials, with predictions consistent with finite element results. Most average errors are below 2%, and peak errors are within 10%. A single prediction takes about 0.35 s, with fluctuations below 0.02 s, improving efficiency by about 90–100 times over conventional finite element analysis. This study provides an effective method for efficient characterization of biaxial tensile full-field mechanical behavior and mechanical performance evaluation of membrane materials under multiple loading conditions.

KEYWORDS: Membrane materials; biaxial tension; mechanical response; finite element analysis; surrogate model

1 Introduction

Membrane materials are high-performance flexible composites and are widely used in tensioned membrane structures, inflatable structures, and lightweight building envelopes [1]. Their mechanical responses under different loading conditions reflect tensile stiffness, anisotropy, nonlinearity, and warp-weft coupling. These responses are essential for evaluating mechanical properties, developing constitutive models, and determining engineering constants [2–4]. Biaxial tensile testing is the main method for obtaining mechanical responses under different warp-to-weft load ratios. However, conventional biaxial tensile results are usually reported as load-displacement curves, stress-strain relationships, or responses at limited measurement points. Such results cannot fully reveal spatial distribution differences, local response concentration, or

Copyright © 2026 The Authors. Published by Tech Science Press. This work is licensed under a Creative Commons Attribution 4.0 International License, which permits unrestricted use, distribution, and reproduction in any medium, provided the original work is properly cited.

deformation-gradient evolution during loading. In contrast, full-field mechanical responses, including stress, strain, and displacement fields, describe the loading and deformation behavior from a spatial perspective. They provide a more complete data basis for material behavior analysis and constitutive model development [5–7].

To overcome the limitations of physical tests in obtaining full-field mechanical responses, constitutive-model-based finite element analysis has become an important approach for studying the mechanical behavior of membrane materials. The finite element method can calculate the stress, strain, and displacement fields of membrane specimens under different loading states based on given material parameters, constitutive relationships, and loading conditions. In this way, the full-field mechanical response of membrane materials can be obtained. Existing studies have mainly focused on constitutive model development, numerical implementation, and finite element applicability. Pargana et al. [8] developed an advanced material model for numerical analysis of coated fabrics, improving the description accuracy of nonlinear mechanical responses in coated fabrics. Minami [9] proposed a multi-step linear approximation method for nonlinear stress-deformation analysis and finite element calculation of coated plain-weave fabrics. Galliot and Luchsinger [10] developed a nonlinear biaxial tensile model for PVC-coated polyester fabrics for finite element applications, enabling the stress-strain relationship under typical load ratios to be characterized more effectively. Chen et al. [11] conducted finite element predictions of the uniaxial and biaxial tensile properties of woven membrane materials, showing that finite element analysis can be used to obtain material responses under different loading conditions. Jekel et al. [12] described PVC-coated polyester as a nonlinear orthotropic material, providing another material representation approach for numerical modeling of coated fabrics. In recent years, more detailed studies have been carried out on load-ratio dependence, damage evolution, and response description under complex loading paths. Yang et al. [13] developed a biaxial tensile constitutive model for PVC-coated fabrics based on a nonlinear orthotropic assumption to characterize warp-weft coupling and nonlinear deformation behavior. Gao et al. [14] proposed a biaxial tensile constitutive model considering shrinkage curves and stress-ratio-dependent coefficients to describe the response characteristics of architectural fabrics under biaxial tension. Zhang et al. [15] established a nonlinear damage constitutive model for PVC-coated fabrics based on continuum damage mechanics to simulate damage evolution and nonlinear responses during tensile loading. Sun et al. [16] developed an efficient constitutive model for coated plain-weave fabrics from the perspective of macro-mesoscopic deformation coupling to predict mechanical behavior in arbitrary loading directions. Pang et al. [17] further proposed a nonlinear biaxial tensile constitutive model considering the effects of stress ratio and strain state to describe material responses of fabric membranes under complex biaxial loading conditions. These studies show that a reasonable constitutive model combined with finite element analysis can reproduce the mechanical responses of membrane materials under different load ratios. It also provides a numerical basis for material behavior analysis and constitutive model evaluation. However, finite element analysis still requires modeling, solving, and post-processing for each loading condition. When multiple constitutive models, numerous biaxial load combinations, and different field variables such as stress, strain, and displacement are involved, repeated calculations substantially increase the time cost. This limits its application efficiency in rapid prediction under multiple loading conditions.

To improve the prediction efficiency of full-field mechanical responses, machine-learning-based finite element surrogate models have gradually been applied to rapid prediction of material and structural mechanical responses. These methods usually use finite element results as training data and learn the mapping relationship between input parameters and output responses. After training, the model can rapidly predict the mechanical response under new loading conditions. Liang et al. [18] were among the first to use deep learning as a fast surrogate model for finite element stress analysis, achieving stress distribution prediction

from geometric and boundary information. Jiang et al. [19] proposed StressGAN, which uses a conditional generative adversarial network to generate two-dimensional stress distributions under geometric, loading, and boundary-condition constraints. Hoq et al. [20] developed data-driven models for full-field stress prediction in random heterogeneous materials. Their work further demonstrates the applicability of machine learning methods to complex material-field prediction. Yang et al. [21] developed an end-to-end deep learning model to predict stress and strain fields in complex hierarchical composites. Bhaduri et al. [22] used a deep convolutional network to predict local stress fields in fiber-reinforced composites, reducing the finite element computational burden in stress analysis of complex microstructures. Mohammadzadeh and Lejeune [23] discussed the feasibility of using deep-learning-based metamodels to predict full-field quantities such as displacement, strain, and damage fields. They pointed out that full-field response prediction is more difficult than single scalar prediction. In addition to convolutional neural networks, graph neural networks and neural operators have also been used for full-field mechanical response prediction. Maurizi et al. [24] mapped finite element meshes into graph structures and developed a graph neural network model to predict deformation, stress, and strain fields in materials. Rashid et al. [25] used a Fourier neural operator to learn stress-strain fields in digital composites, demonstrating the potential of neural operators for field prediction in complex materials. In addition, reduced-order surrogate modeling methods that combine autoencoders and regression models have attracted increasing attention. Deshpande et al. [26] used an autoencoder to compress high-dimensional finite element displacement fields and used Gaussian process regression to establish the mapping between input loads and low-dimensional displacement representations. This study provided an effective idea for predicting high-dimensional finite element solutions in a low-dimensional latent space. Xu et al. [27] proposed a CAE-DNN model to predict the full-field stress of tensioned membrane structures. Their study demonstrated the feasibility of combining a CAE with a nonlinear regression model for rapid stress-field prediction. These studies show that finite element surrogate models can significantly improve the prediction efficiency of complex mechanical fields and provide a feasible approach for rapid multi-condition analysis. In an autoencoder-based reduced-order surrogate modeling framework, the nonlinear regression layer determines the mapping accuracy from input parameters to latent codes. Different regression models vary in modeling strategy, nonlinear representation capability, and prediction stability. Therefore, they may produce different prediction results for the same type of data. Therefore, developing a finite element surrogate model suitable for predicting the full-field mechanical response of membrane materials under biaxial tension is of great importance. Such a model can rapidly and stably obtain accurate full-field responses, which are essential for evaluating the mechanical properties of membrane materials and establishing material constitutive models.

This study focuses on the full-field mechanical response of membrane materials under biaxial tension. Based on a comparative analysis of existing regression models, a CAE-ET finite element surrogate model integrating a convolutional autoencoder and extremely randomized trees is proposed. First, a biaxial tensile finite element dataset is constructed based on two representative constitutive models, namely orthotropic and hyperelastic models, and the reliability of the finite element model is verified using experimental results. Then, a CAE-ET surrogate prediction framework is established and compared with DNN and LSTM regression models to evaluate the applicability of different regressors in low-dimensional latent-code prediction. On this basis, the prediction performance of the proposed model is analyzed for stress, strain, and displacement fields under the two constitutive conditions. Its accuracy and efficiency are further evaluated in terms of average error, peak error, and computation time. Building on existing autoencoder-based surrogate modeling approaches, this study aims to develop a framework that is more suitable for the rapid prediction of full-field mechanical responses of membrane materials under biaxial loading, thereby improving both the efficiency and accuracy of acquiring full-field mechanical information.

2 Materials and Methods

The overall workflow of the proposed framework is shown in Fig. 1. The framework combines the CAE and ET models to predict the full-field mechanical responses of membrane materials with different constitutive models under biaxial tension. First, finite element analysis was performed to obtain the stress, strain, and displacement fields under given constitutive parameters and biaxial loading conditions. These field responses were then converted into multichannel matrix data and used as training samples for the model. After training, the CAE-ET model first maps the input constitutive information and biaxial loading conditions into low-dimensional latent codes through ET. The CAE decoder then reconstructs these latent codes into stress, strain, and displacement fields, thereby obtaining the full-field mechanical response of the membrane material under the corresponding loading condition.

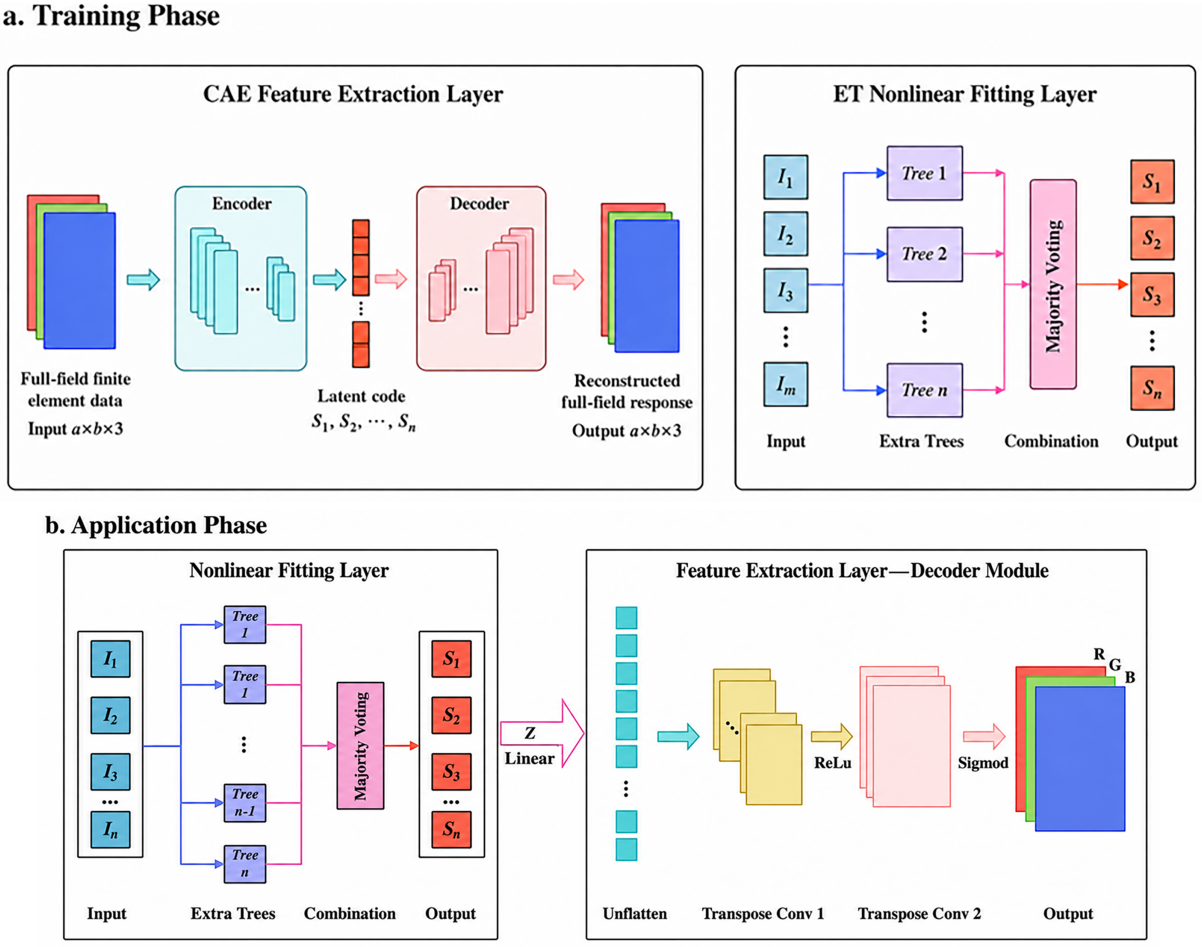


Figure 1: Schematic diagram of the model workflow: (**a**) Training stage; (**b**) Application stage.

2.1 Dataset

2.1.1 Dataset Construction

The dataset used for training, validation, and testing of the data-driven prediction model was constructed from ABAQUS finite element simulation results.

The finite element model of the cross-shaped specimen is shown in Fig. 2. The complete specimen had planar dimensions of 480 mm × 480 mm, with a central loading region of 160 mm × 160 mm, a loading-arm width of 160 mm, and an end-clamping length of 50 mm. The specimen geometry was symmetric about both the vertical centerline $x = 0$ and the horizontal centerline $y = 0$. In the x-direction, equal and opposite tensile loads CF_x were applied to the left and right sides of the specimen, while equal and opposite tensile loads CF_y were applied to the upper and lower sides in the y-direction. Considering the symmetry of the specimen geometry, material orientations, and loading configuration, the upper-right quarter of the complete specimen was used in the finite element analysis to reduce the computational scale. Corresponding symmetry boundary conditions were applied along the two symmetry axes. The external loads were also reduced according to the symmetry relation to ensure mechanical equivalence between the quarter and complete models. This simplification reduced the computational cost and improved the efficiency of multi-condition finite element analyses and training-data generation while preserving the mechanical response of the complete model. The model was discretized using CPS3 three-node plane-stress triangular elements, with a uniform thickness of t = 0.66 mm. The region used for field-variable extraction in the quarter model contained 640 CPS3 elements and 489 nodes. Two constitutive models were used in the finite element calculations: the orthotropic constitutive model available in ABAQUS and the fiber-reinforced anisotropic hyperelastic model proposed by Xu et al. [28] for architectural PTFE-coated fabrics. The latter describes the anisotropic nonlinear response of membrane materials through the strain-energy contributions of the matrix, warp and weft yarn stretching, and warp–weft interaction, and was implemented in ABAQUS using a VUMAT user-material subroutine. The corresponding material parameters are listed in Tables 1 and 2. The unit "1" assigned to k_{21} and k_{22} in Table 2 indicates that these parameters are dimensionless. Biaxial tensile loads were applied along the warp and weft directions of the specimen. The load range was 1400–12,600 N, with an increment of 1400 N. A total of 81 load-ratio conditions were designed in the two directions, including 1:1, 1:2, . . ., 1:9, 2:1, . . ., and 9:9.

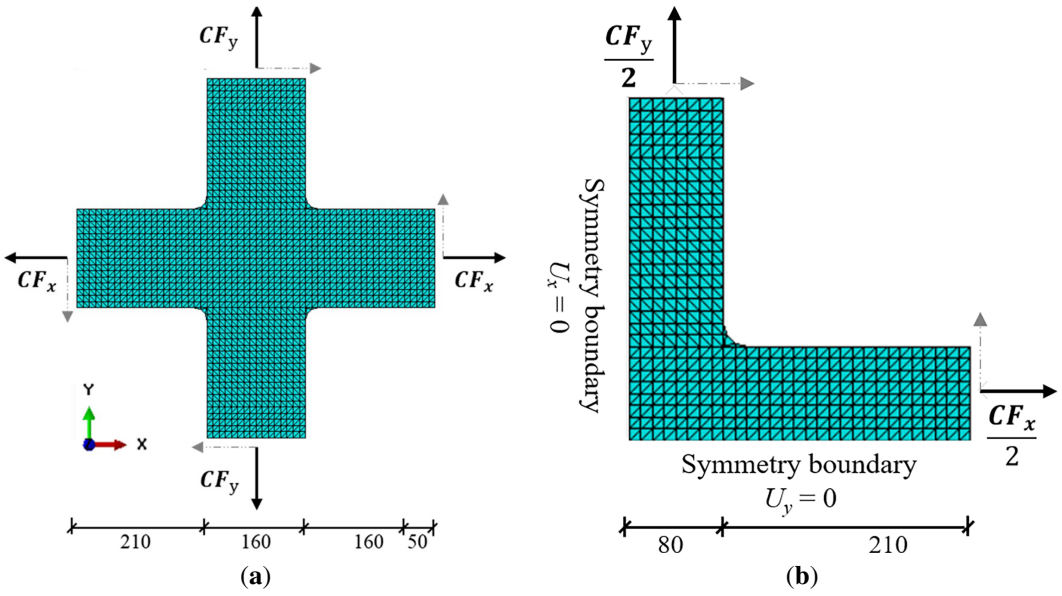


Figure 2: Finite element model of the cross-shaped specimen (unit: mm): (**a**) full finite element model; (**b**) quarter finite element model.

Table 1: Material parameters of coated fabric membranes for the orthotropic constitutive model.

μ	E_1 (MPa)	E_2 (MPa)	G_{12} (MPa)	G_{13} (MPa)	G_{23} (MPa)
0.3	1600	1500	278	278	37

Table 2: Material parameters of coated fabric membranes for the hyperelastic constitutive model [28].

M (kN/m)	k_{11} (kN/m)	k_{12} (kN/m)	k_{21} (1)	k_{22} (1)	k_{31} (kN/m)	k_{32} (kN/m)
288.83	217.74	6.19	106.11	1133.50	118.49	123.47

To verify the appropriateness of the selected element type, comparative analyses were conducted using CPS3, CPS4, and CPS6 elements. The specimen geometry, material parameters, membrane thickness, boundary conditions, and loading configuration were kept unchanged, as shown in Fig. 3. A mesh-size sensitivity analysis was also performed for the finite element model developed in this study. The plane tensioned membrane structure model was discretized using three different element sizes of 3, 4, and 6 mm, and the displacement results obtained from the different models were compared, as shown in Fig. 4. As shown in the figures, the displacement fields obtained using different element types and mesh sizes were generally consistent in terms of the overall distribution pattern and the locations of the extrema. No obvious differences in the calculated results were caused by the use of different element types or mesh sizes. These results confirm that the selected element type and mesh size were appropriate.

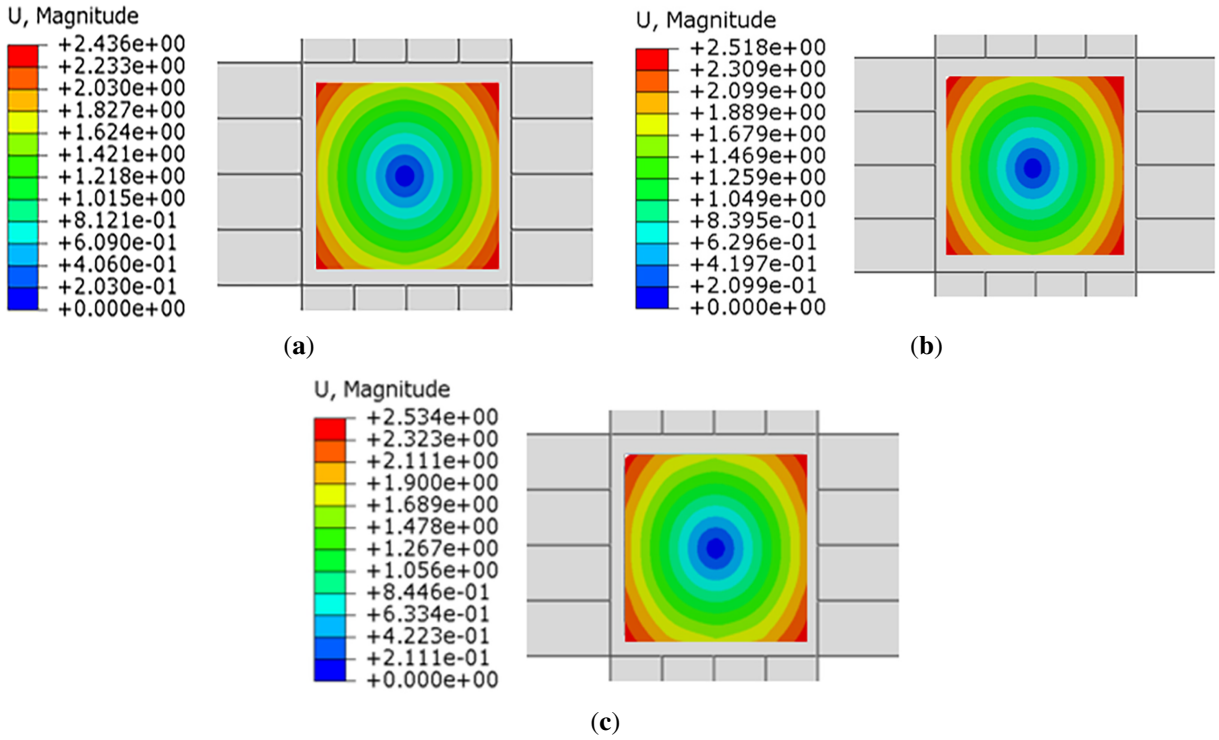


Figure 3: Analysis results using different element types: (**a**) Displacement contour plot for the 3 mm mesh; (**b**) Displacement contour plot for the 4 mm mesh; (**c**) Displacement contour plot for the 6 mm mesh.

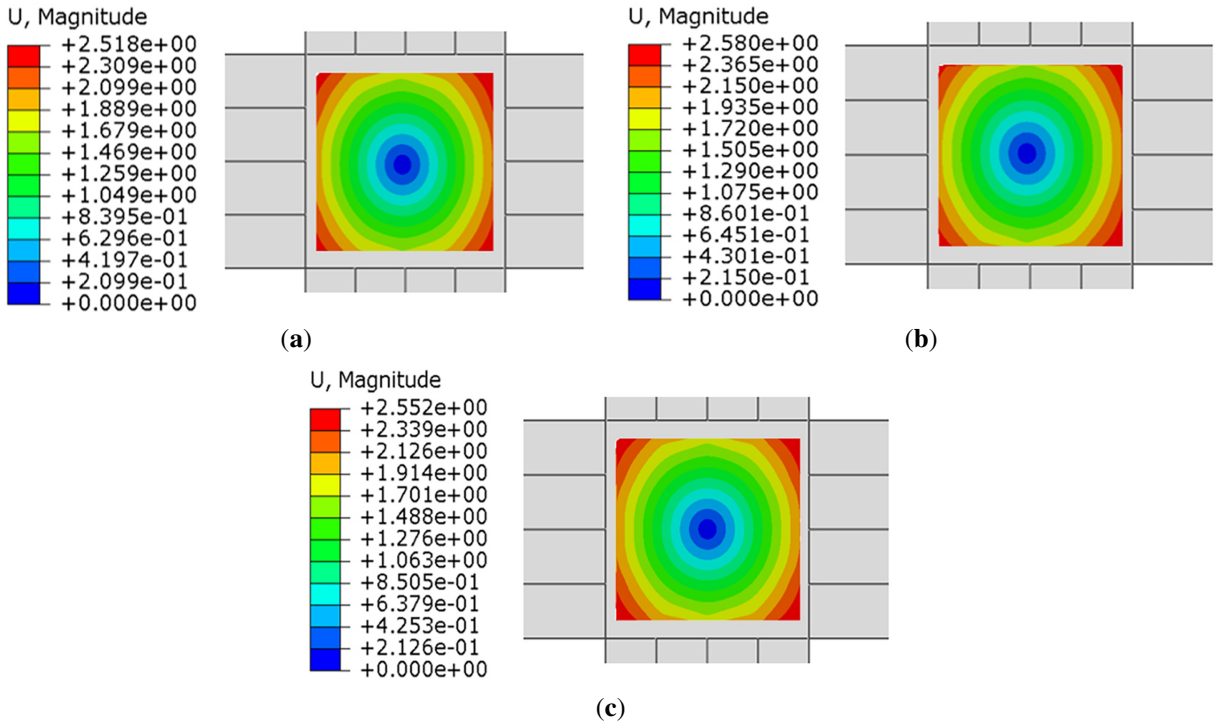


Figure 4: Element size sensitivity analysis results: (**a**) Displacement contour plot for the model meshed with CPS3 elements; (**b**) Displacement contour plot for the model meshed with CPS4 elements; (**c**) Displacement contour plot for the model meshed with CPS6 elements.

To match the input format of the convolutional autoencoder, a custom Abaqus Python post-processing and data-preprocessing program was used to extract element stress, element strain, and nodal displacement data frame by frame from the ODB files generated by the finite element analyses. The extracted data were then converted into regular multichannel data matrices. Different physical components were stored in different channels. The number of finite elements corresponded one-to-one to the number of pixels, as shown in Fig. 5, where the gray regions represent the clamped regions. This conversion changed only the data organization form and did not change the numerical magnitude relation among components. Because the cross-shaped specimen was discretized using 640 CPS3 elements, the two-dimensional mapping size of the stress and strain data was set to $32 \times 20 \times 3$. In the EXR channel mapping, the R channel corresponded to S11 (X-direction normal stress) and E11 (X-direction normal strain), the G channel corresponded to S22 (Y-direction normal stress) and E22 (Y-direction normal strain), and the B channel corresponded to S12 (XY-direction shear stress) and E12 (XY-direction shear strain). For the nodal displacement data, the finite element mesh contained 489 nodes. To obtain a rectangular image with a more balanced aspect ratio and improve data storage and processing efficiency, five blank entries were added during data conversion. The final EXR image size was therefore set to $19 \times 26 \times 3$. Because the cross-shaped specimen was subjected to in-plane tension, no out-of-plane displacement or Z-direction displacement component existed. Therefore, in the channel mapping, the R channel stored U1 (X-direction displacement), the G channel stored U2 (Y-direction displacement), and the B channel was left empty.

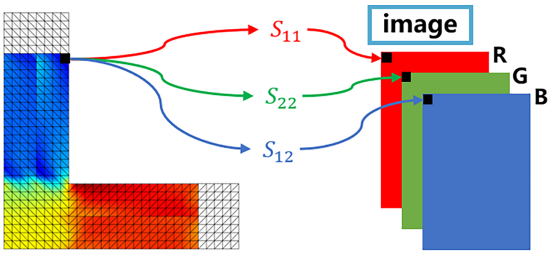


Figure 5: Schematic mapping between finite elements and image pixels.

To reduce the risk of overfitting and objectively evaluate model performance, the dataset was divided into separate training, validation, and test sets. Approximately 8000 training samples were used for model parameter learning and for updating the network weights and biases. Approximately 2000 validation samples were excluded from parameter updates. They were used to calculate the validation loss, monitor model convergence, assist in detecting overfitting, and support model selection. Approximately 2000 test samples were kept isolated during model training, hyperparameter tuning, and model selection. They were used only after the final model had been determined to evaluate the prediction accuracy and generalization performance on unseen samples. These samples covered the prescribed biaxial load combinations and the mechanical responses at different loading stages. They provided the data basis for learning the main spatial variation characteristics of the full-field responses within the scope of this study.

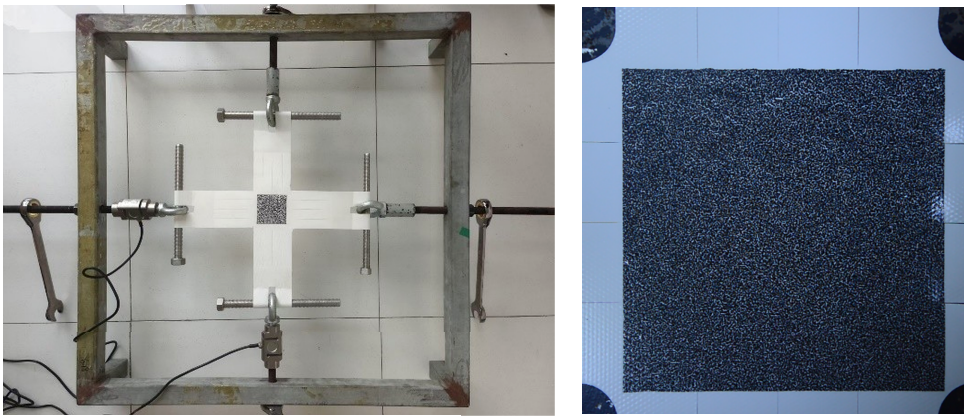
2.1.2 Reliability Verification

The training samples and prediction accuracy evaluation of the CAE-ET model in this study are both based on finite element calculation results. Therefore, the reliability of the finite element results directly affects the credibility of the subsequent model validation conclusions. It is necessary to verify the calculation results of the finite element model to show that the model can reasonably reflect the mechanical response characteristics of membrane materials under biaxial tension.

The cross-shaped planar tensioned membrane specimen used in the test had a design size of 480 mm × 480 mm. The overall layout adopted a standard specimen design with a central square loading region and clamped regions on four sides. The clamped region width was 160 mm, and the clamping length was set to 50 mm. The core region was a 160 mm × 160 mm square loaded region, consistent with the geometry described in Section 2.1.1. The mechanical parameters of the tested membrane material are listed in Table 3, while the corresponding constitutive parameters used in the finite element model are listed in Table 2. The test setup is shown in Fig. 6. A load ratio of 1:0 was adopted. Before testing, the surface of the core region was cleaned. After the background coating had dried, black acrylic paint was randomly sprayed to form speckles of different sizes and spacings, producing a high-contrast black-and-white speckle pattern over the core region. During loading, a high-resolution camera continuously recorded the deformation of the speckle pattern. The recorded image sequence was then processed using the Ncorr V1.2 digital image correlation software. Full-field displacement and strain data in the core region were obtained and compared with the finite element results under the same loading condition to validate the accuracy of the finite element model.

Table 3: Basic parameters of the tested membrane material.

Type	Manufacturer	Grade	Areal Density (g/m^2)	Thickness (mm)	Tensile Strength (N/5 cm)		Tear Strength (N)	
					Warp	Weft	Warp	Weft
TB6K	Huifeng	G6	1118	0.66	7138	6150	509	476



(**a**) (**b**)

Figure 6: Biaxial tensile test platform for the cross-shaped specimen: (**a**) Test setup; (**b**) Speckle pattern on the cross-shaped specimen.

2.2 CAE-ET Prediction Model

2.2.1 Feature Extraction Layer

The feature extraction layer used a convolutional autoencoder to achieve low-dimensional encoding and reconstruction of finite element mechanical field responses. The convolutional autoencoder consisted of an encoder and a decoder, as shown in Fig. 7. Compared with a conventional autoencoder, a convolutional autoencoder can extract local spatial features using convolution kernels. It is more suitable for stress, strain, and displacement fields with clear spatial correlation. The response fields of membrane specimens usually exhibit continuous distributions, local concentration, and gradient variation. Convolution operations can capture these spatial patterns and compress them into low-dimensional feature codes. This reduces the output dimension of the subsequent nonlinear regression model.

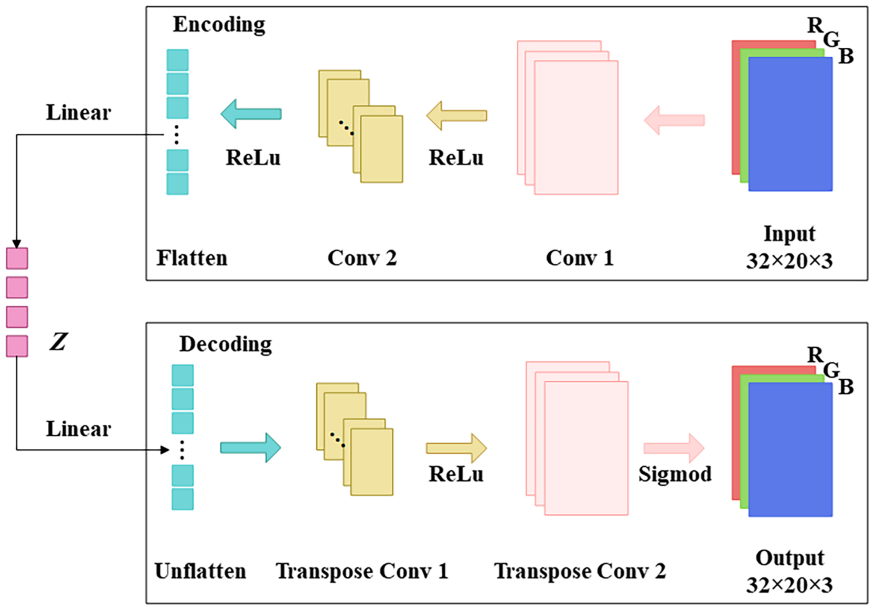


Figure 7: Feature extraction layer.

In neural networks, activation functions enhance the representation and learning abilities of the network. They apply nonlinear transformations to neuron inputs, allowing the network to learn complex patterns and features. The activation functions used in this study are Sigmoid and ReLU, and their expressions are given in Eqs. (1) and (2), respectively [29,30].

$$\mathrm{S}(x) = \frac{1}{1+e^{-x}} \tag{1}$$

$$\mathrm{R}(x) = \max(0, x) \tag{2}$$

To enable the CAE to balance pixel-level accuracy and structural integrity during image reconstruction, this study used the structural similarity index measure (SSIM) proposed by Wang et al. [31]. A comprehensive loss function combining mean squared error (MSE) and SSIM was then constructed, as expressed in Eq. (3).

$$F_{Loss} = \mathrm{MSE}_1 + \mathrm{MSE}_2 + \mathrm{MSE}_3 + 1 - \mathrm{SSIM} \tag{3}$$

The expressions of MSE and SSIM are given in Eqs. (4) and (5), respectively.

$$\mathrm{MSE} = \frac{1}{m \times n} \sum \left(I(i,j) - G(i,j)\right)^2 \tag{4}$$

where $I(i,j)$ and $G(i,j)$ denote the values of the input and reconstructed matrices, respectively, at the i-th row and j-th column, and m and n denote the numbers of rows and columns, respectively.

$$\mathrm{SSIM} = \frac{(2 \times \mu_I \times \mu_G + c_1) \times (2 \times \sigma_{IG} + c_2)}{\left(\mu_I^2 + \mu_G^2 + c_1\right) \times \left(\sigma_I^2 + \sigma_G^2 + c_2\right)} \tag{5}$$

where μ_I and μ_G denote the mean values of the input and reconstructed fields, respectively; σ_I^2 and σ_G^2 denote their variances; σ_{IG} denotes the covariance between the input and reconstructed fields; c_1 and c_2 are positive constants.

2.2.2 Nonlinear Fitting Layer

The nonlinear fitting layer was used to establish the mapping between input variables and low-dimensional feature codes. In this study, extremely randomized trees (ET) were used as the regression model for CAE low-dimensional feature codes. The ET model consisted of 50 extremely randomized regression trees. Each regression tree predicted the four-dimensional latent code of the CAE, and the final prediction was obtained by taking the arithmetic mean of the outputs of all 50 trees. The structure of the ET algorithm is shown in Fig. 8.

Extremely randomized trees are a nonlinear regression method based on decision tree ensembles. Compared with conventional random forests, ET introduces stronger randomness during node splitting. This can reduce model variance and improve training efficiency. Compared with DNN and LSTM models that rely on backpropagation optimization, ET is less sensitive to hyperparameters. It also has good stability in the low-dimensional feature space. Because the CAE compressed high-dimensional field variables into low-dimensional feature codes, ET only needed to learn the mapping between limited input variables and low-dimensional feature codes. Therefore, ET is suitable for the hierarchical prediction framework in this study.

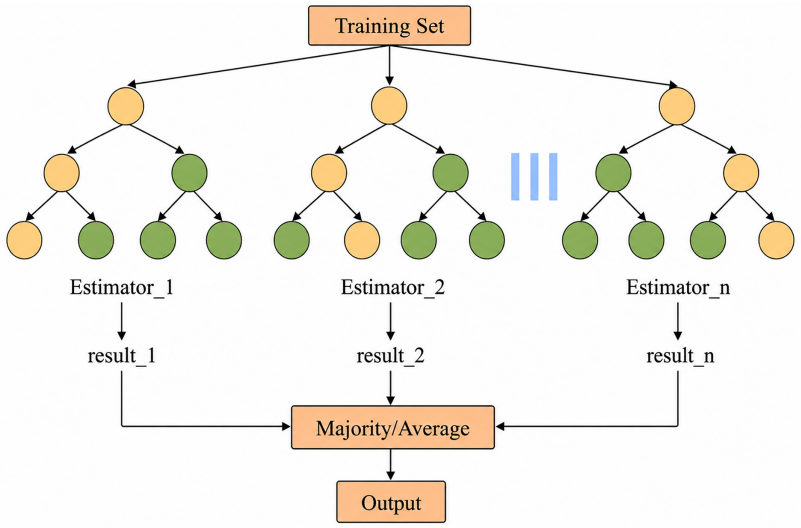


Figure 8: Structure of the extremely randomized trees (ET) algorithm.

2.3 Regression Evaluation Metrics

To comprehensively evaluate the prediction performance of the model for structural mechanical field responses, an evaluation system was established from two aspects: code regression accuracy and field distribution accuracy. For code regression accuracy, mean squared error (MSE), determination R^2, and mean absolute error (MAE) were used. These metrics measured the mapping ability of the nonlinear fitting layer for code vectors. Lower MSE and a higher R^2 and lower MAE indicate better fitting accuracy for low-dimensional feature codes. The expressions are given in Eqs. (4), (6) and (7).

$$R^2 = 1 - \frac{\sum_{i=1}^{m}(y_i' - y_i)^2}{\sum_{i=1}^{m}(\overline{y}_i - y_i)^2} \tag{6}$$

$$\mathrm{MAE} = \frac{1}{m}\sum_{i=1}^{m}|y_i' - y_i| \tag{7}$$

For the prediction effects of stress, strain, and displacement fields, normalized mean absolute error (NMAE) and normalized absolute error (NAE) were further introduced. NMAE was defined as the ratio of the mean absolute error between predicted and true values to the maximum absolute true value. It was used to reflect the average error level of the mechanical field, as expressed in Eq. (8). NAE measured the peak-capturing ability of the model by comparing the relative deviation between predicted and true peak values. Its expressions are given in Eqs. (9) and (10). The combination of the two metrics can comprehensively evaluate the reconstruction accuracy of structural mechanical response fields.

$$\mathrm{NMAE} = \frac{\mathrm{MAE}}{max\{|S|\}} \times 100\% \tag{8}$$

$$\mathrm{AE} = |\max\{|S|\} - \max\{|\overline{S}|\}| \tag{9}$$

$$\mathrm{NAE} = \frac{\mathrm{AE}}{max\{|S|\}} \times 100\% \tag{10}$$

3 Results and Discussion

3.1 Reliability Analysis of the Finite Element Model

Fig. 9 shows the experimental DIC displacement fields and finite element displacement fields in the core region under a load ratio of 1:0. The DIC test results and finite element results showed good agreement in both warp- and weft-direction displacement fields. For warp-direction displacement, the DIC results showed that displacement in the core region gradually changed from negative values on the left to positive values on the right. The zero-displacement band was located near the middle of the specimen. The finite element U1 displacement field also showed a continuously increasing distribution from left to right. The locations of positive and negative displacement regions, the zero-displacement transition region, and the overall gradient direction were basically consistent with the experimental results. For weft-direction displacement, the DIC results showed that displacement gradually changed from negative values at the bottom to positive values at the top. The finite element U2 displacement field also showed the same upper-lower partition and vertical gradient variation. This indicates that the finite element model reproduced the biaxial tensile deformation characteristics of the core loaded region well.

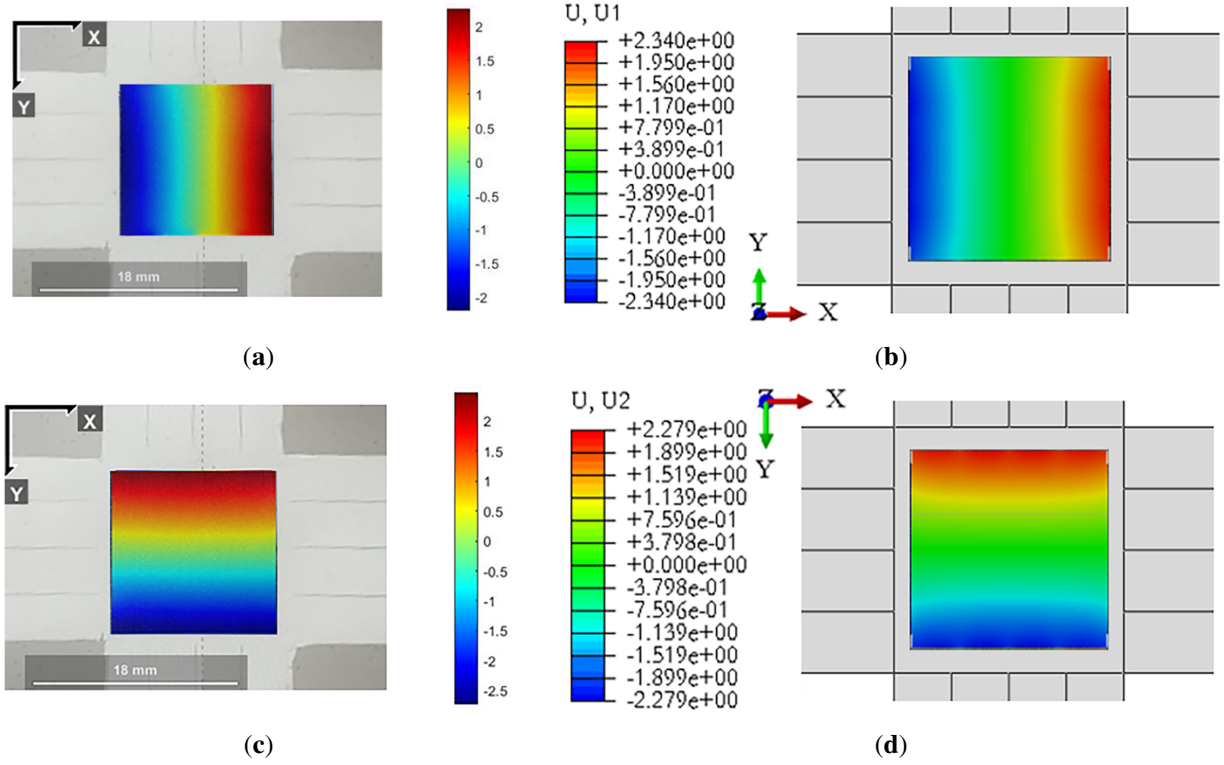


Figure 9: Comparison of finite element and experimental displacement contour maps in the core region under a 1:0 load ratio (unit: mm): (**a**) Experimental result of warp-direction displacement; (**b**) Finite element result of warp-direction displacement; (**c**) Experimental result of weft-direction displacement; (**d**) Finite element result of weft-direction displacement.

Fig. 10 further compares the experimental and finite element logarithmic strain fields under the same loading condition. The warp-direction strain was positive throughout the core region, with relatively high values mainly concentrated in the central area and lower values distributed around parts of the boundary. The finite element LE11 field reproduced the same overall distribution characteristics. In the weft direction, both the experimental and finite element LE22 fields were negative, indicating transverse contraction under

warp-direction loading. The relatively large compressive strains were mainly concentrated in the central region, while their absolute values gradually decreased toward the surrounding boundaries. Although the experimental strain fields exhibited more local fluctuations than the finite element results, the overall distributions and the locations of the principal high- and low-strain regions were generally consistent.

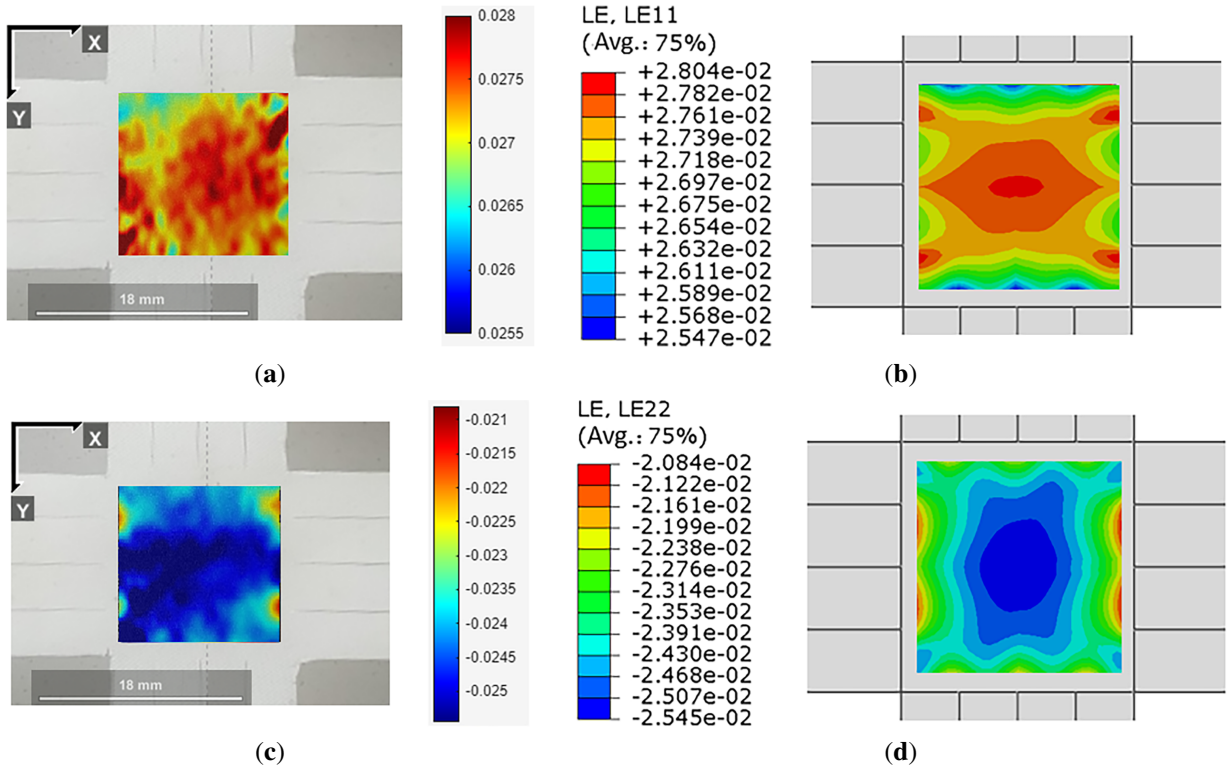


Figure 10: Comparison of finite element and experimental logarithmic strain contour maps in the core region under a 1:0 load ratio: (**a**) Experimental result of warp-direction strain; (**b**) Finite element result of warp-direction logarithmic strain; (**c**) Experimental result of weft-direction strain; (**d**) Finite element result of weft-direction logarithmic strain.

In terms of displacement magnitude, the warp-direction displacement in the DIC test was mainly distributed within −2 to 2 mm. The finite element U1 displacement range was about −2.34 to 2.34 mm. The weft-direction displacement in the DIC test was distributed approximately within −2.5 to 2 mm. The finite element U2 displacement range was about −2.279 to 2.279 mm. In terms of strain magnitude, the experimental warp-direction strain ranged approximately from 0.0255 to 0.0280, while the finite element LE11 strain ranged from 0.02547 to 0.02804. The experimental weft-direction strain ranged approximately from −0.0250 to −0.0210, while the finite element LE22 strain ranged from −0.02545 to −0.02084. The experimental and finite element results were therefore consistent not only in the displacement and strain distribution patterns but also in their overall magnitudes. Local differences between the experimental and finite element results may have resulted from fixture constraints, local material nonuniformity, slight slip at the clamped ends, DIC measurement fluctuations, and idealized finite element boundary conditions. In particular, the experimental strain fields showed more local fluctuations, whereas the finite element strain fields were relatively smooth because homogeneous material properties and idealized loading and boundary conditions were adopted in the numerical model. However, the overall deformation trends and the displacement and strain field distributions did not show obvious deviations. Therefore, the finite element

model established in this study can reasonably represent the mechanical response of the membrane material. It can be used as the reference solution for evaluating the prediction performance of the CAE-ET model.

3.2 Training Results of the Feature Extraction Layer

To validate the compression and reconstruction ability of the CAE for mechanical field stress data, the stress field data of the cross-shaped specimen were used as training objects. The training process and reconstruction effect of the feature extraction layer were then analyzed. The input was a three-channel stress image with a size of 32 × 20 × 3. The three channels corresponded to the stress components S11, S22, and S12, respectively. The channel-first format in PyTorch was used inside the network. The CAE used in this study consisted of an encoder and a decoder. The encoder included two 2D dimensional convolutional layers, ReLU activation functions, a Flatten layer, and a fully connected layer in sequence. It compressed the input image into a 4-dimensional latent feature code. The decoder consisted of a fully connected layer, an Unflatten layer, and two two-dimensional transposed convolutional layers. It reconstructed the 4-dimensional latent code into a three-channel mechanical field image with the same size as the input.

Fig. 11 shows the loss curves of the CAE model and the evolution of the reconstructed matrices during training. The reconstructed matrices correspond to the same fixed sample at epochs 10, 50, 100, and 200, while "Input" on the far right represents the reference input matrix of this sample. These results provide an intuitive view of the convergence behavior of the feature extraction layer. The maximum number of training epochs for the CAE was set to 400. The validation loss decreased rapidly from about 0.15 to about 0.06 within the first 10 epochs. It then gradually converged to around 0.01 after about 200 epochs. The loss curves remained stable afterward, and no obvious divergence between the training and validation losses was observed. This indicates that the CAE achieved good convergence and reconstruction stability under the training-validation split and loss function settings used in this study.

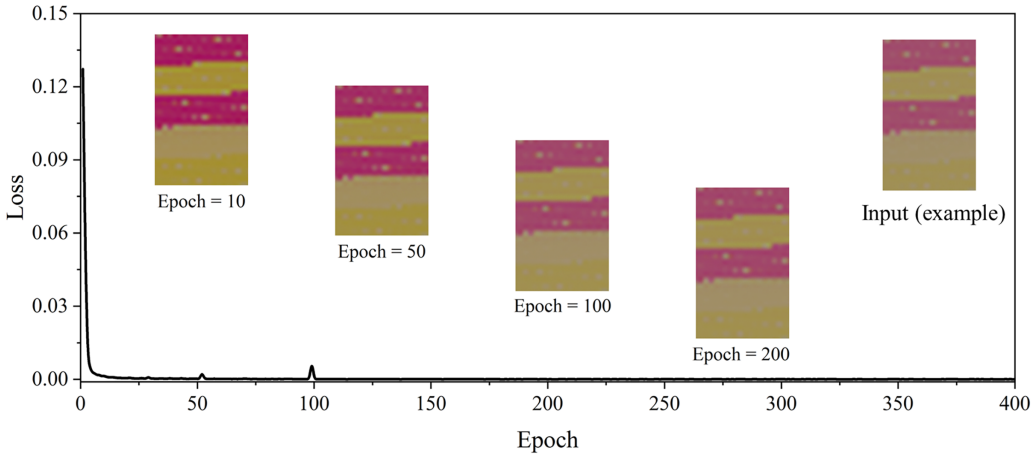


Figure 11: Model loss curves and changes in reconstructed matrices during training.

Fig. 12 shows the input and output results of the feature extraction layer, demonstrating the ability of the CAE to reconstruct stress field images. The reconstructed images reproduced the structural features and edge distributions of the original images well. The three rows correspond to three independent representative input samples. These samples mainly differ in their brightness distributions, including the locations of bright and dark regions and their relative contrast. Because the EXR images were used to store normalized physical field data, the image brightness represents the relative magnitude of the normalized physical quantities at different locations. The three samples with different brightness distributions were selected to examine

whether the CAE could recover both the overall intensity relationships and local details of the input fields under different grayscale distributions. The quantitative results showed that all SSIM values were not lower than 0.989, and the maximum MSE did not exceed 0.800. These results indicate that the CAE can accurately reconstruct the input images. It also has the ability to reconstruct stress matrices from low-dimensional feature codes.

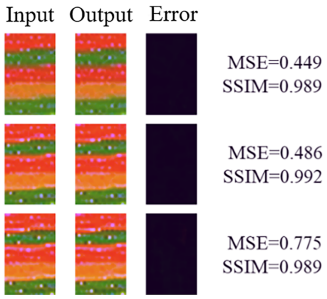


Figure 12: Input-output pairs of the feature extraction layer.

3.3 Training Results of the Nonlinear Fitting Layer

The CAE can only encode and reconstruct known finite element response fields and cannot directly generate unknown response fields from new material parameters and loading conditions. The nonlinear fitting layer establishes the nonlinear mapping between the material parameters and biaxial loading conditions and the low-dimensional latent codes of the CAE. It therefore serves as a key link between the input conditions and the full-field mechanical response outputs. To analyze the applicability of different regression models for the present dataset under a unified evaluation procedure, three representative regression models with different modeling mechanisms, namely DNN, LSTM, and ET, were selected for comparison. All three models used the model parameters and loading conditions as inputs, and the low-dimensional latent codes output by the CAE encoder were used as regression targets. Model performance was evaluated using K-fold cross-validation, with K set to 5. The evaluation metrics were R^2, MAE, and MSE. The model comparison in this section aimed to evaluate the applicability of different regressors for CAE latent-code mapping. It was not intended to rank their theoretical optimal performance. DNN, LSTM, and ET correspond to different model assumptions, parameter update strategies, and hyperparameter spaces. Therefore, complete equivalence in structural complexity and optimization intensity cannot be ensured using a single evaluation metric. The comparison was conducted under the same training samples, input-output variables, cross-validation splits, and evaluation metrics. This design minimized the influence of data division and evaluation method on the comparison results.

The five-fold cross-validation results of the three models in Tables 4–6 showed that the test-set R^2 values of DNN, LSTM, and ET were 0.9918, 0.9938, and 0.9995, respectively. All values reached high levels, indicating that the three models could effectively learn the mapping between input variables and CAE low-dimensional feature codes. Among them, the MAE and MSE of the ET model on the test set were 6.667×10^{-4} and 1.656×10^{-6}, respectively, which are significantly lower than those of DNN and LSTM. In addition, the training-set R^2 of the ET model remained between 0.9993 and 0.9999, whereas the training-set R^2 of DNN and LSTM showed larger fluctuations. This indicates that, under the current limited sample size and low-dimensional coding prediction task in this study, the ET model could more accurately capture the nonlinear relationship between the input variables and the latent codes. The better performance of ET under the present settings was closely related to the characteristics of the prediction task. The inputs consisted of material parameters and loading conditions in the warp and weft directions, which were low-dimensional

and non-sequential, while the output was the four-dimensional latent code extracted by the CAE. ET could partition and fit the nonlinear relationships in the input space using multiple randomized regression trees. Ensemble averaging also reduced the prediction fluctuations caused by individual trees and specific data splits. In contrast, although DNN has strong nonlinear expressive ability, its performance is greatly affected by hyperparameters such as network structure, learning rate, regularization method, and training epochs. When the number of samples is limited, DNN may have difficulty fully exploiting the expressive advantages of deep networks, and the training process is more easily affected by local optima, parameter initialization, and sample distribution. LSTM is mainly suitable for data modeling with clear temporal dependence or sequential evolution characteristics, whereas the input variables in this study mainly consist of material parameters and loading conditions and do not have a typical time-series structure. Therefore, the compatibility between its model structure and the latent-code regression task in this study is relatively limited, and it fails to show an obvious advantage.

Table 4: Training results of the DNN model.

	Training Set			Test Set		
Fold	**MAE**	**MSE**	**R^2**	**MAE**	**MSE**	**R^2**
1	1.104×10^{-2}	2.041×10^{-4}	0.9917			
2	1.087×10^{-2}	1.942×10^{-4}	0.9933			
3	1.486×10^{-2}	3.515×10^{-4}	0.9861	1.221×10^{-2}	2.389×10^{-4}	0.9918
4	8.862×10^{-3}	1.412×10^{-4}	0.9938			
5	1.176×10^{-2}	2.249×10^{-4}	0.9916			

Table 5: Training results of the LSTM model.

	Training Set			Test Set		
Fold	**MAE**	**MSE**	**R^2**	**MAE**	**MSE**	**R^2**
1	1.307×10^{-2}	5.943×10^{-4}	0.9945			
2	1.362×10^{-2}	6.124×10^{-4}	0.9942			
3	1.418×10^{-2}	6.431×10^{-4}	0.9938	1.421×10^{-2}	6.375×10^{-4}	0.9938
4	1.389×10^{-2}	6.286×10^{-4}	0.9940			
5	1.452×10^{-2}	6.692×10^{-4}	0.9935			

Table 6: Training results of the ET model.

	Training Set			Test Set		
Fold	**MAE**	**MSE**	**R^2**	**MAE**	**MSE**	**R^2**
1	8.039×10^{-4}	2.078×10^{-6}	0.9994			
2	7.535×10^{-4}	1.781×10^{-6}	0.9995			
3	7.992×10^{-4}	2.653×10^{-6}	0.9999	6.667×10^{-4}	1.656×10^{-6}	0.9995
4	7.128×10^{-4}	2.377×10^{-6}	0.9993			
5	9.078×10^{-4}	1.261×10^{-6}	0.9996			

Fig. 13 shows the true and predicted stress codes on the test set. The stress-field latent code was a four-dimensional feature vector obtained by compressing the three-channel stress input tensor through the CAE encoder. This vector comprehensively represented the spatial distribution characteristics of the stress field. The reference latent codes in Fig. 13 were obtained by encoding the true stress fields using the CAE encoder, whereas the predicted latent codes were generated by ET from the material parameters and loading conditions. The figure therefore illustrates the regression performance of the ET model for low-dimensional latent codes. The scatter points of the true and predicted values were closely distributed around the y = x line, with no obvious dispersion. They extended uniformly from low to high values along the y = x line, indicating that the ET model produced small overall prediction errors for the low-dimensional feature codes.

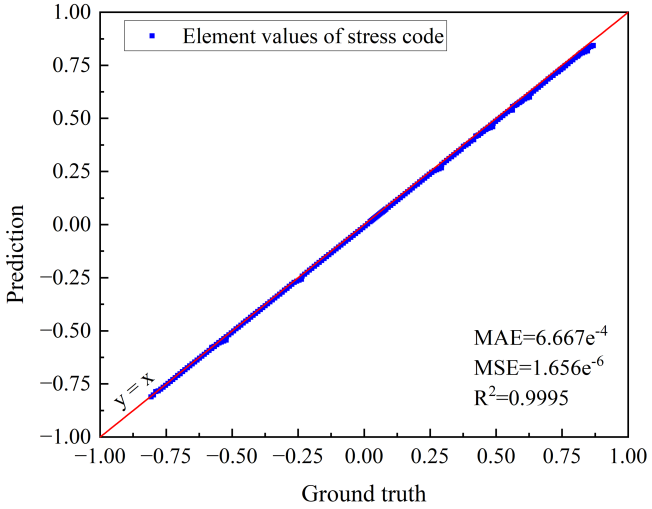


Figure 13: Comparison between true and predicted stress codes.

Based on the above results, ET was selected as the nonlinear mapping model for the CAE latent codes. Its high regression accuracy and small cross-validation fluctuations on the test set helped limit the propagation of latent-code prediction errors during decoding. This improved the consistency and stability of the reconstructed full-field mechanical responses under different loading conditions. The resulting CAE-ET model can rapidly predict the corresponding full-field stress, strain, and displacement responses from the material parameters and warp- and weft-direction loading conditions. It therefore provides a surrogate modeling approach that balances computational efficiency and prediction accuracy for multi-condition prediction, parameter sensitivity analysis, and load-combination screening of membrane materials under biaxial loading. Owing to the research objectives and the requirements of a unified comparison, a systematic benchmark analysis covering a wider range of surrogate models was not conducted in this study. Therefore, the present results only demonstrate the suitability of ET under the compared models, dataset size, and evaluation conditions considered in this study, rather than its universal superiority over other algorithms.

3.4 Prediction Performance Validation of the CAE-ET Model

The cross-shaped membrane specimen was used as the validation object in this study. Typical samples under orthotropic and hyperelastic constitutive conditions were selected separately. The stress, strain, and displacement fields predicted by the CAE-ET model were compared with finite element results. NMAE and NAE were used to quantitatively evaluate the average error and peak error. This validated the ability of the CAE-ET model to predict full-field mechanical responses of membrane materials under plane biaxial tensile

conditions with different load ratios. To ensure the objectivity of generalization performance evaluation, the selected validation samples were not used in model training.

3.4.1 Prediction Performance for Orthotropic Membrane Materials

In this section, a cross-shaped specimen of orthotropic coated fabric membrane material was selected as the validation object. The material parameters are listed in Table 1. Four typical load-ratio conditions were selected: 1:1, 9:9, 1:5, and 5:1. The stress, strain, and displacement fields predicted by the CAE-ET model were validated and compared with corresponding finite element results. The prediction performance of the model under the orthotropic constitutive condition was evaluated in terms of the stress, strain, and displacement fields.

Figs. 14 and 15 show the stress field prediction results and the corresponding NMAE and NAE curves for orthotropic membrane materials under different load ratios. The stress contour maps of orthotropic membrane materials predicted by the CAE-ET model under different load ratios were highly consistent with the finite element contour maps. The agreement was observed in the overall distribution pattern, local peak positions, and stress concentration regions. Under the 1:5, 5:1, and 1:1 tensile conditions, the maximum NMAE was 0.30%, and the maximum NAE was 2.35%. This indicates that the model maintained high stress-field prediction accuracy under both symmetric and asymmetric loading modes. Under the 9:9 tensile condition, the stress peak increased to 492.41 MPa, and the local gradient of the stress field became steeper. The model had greater difficulty capturing such high-amplitude extreme features, causing NAE to increase to 6.51%. Nevertheless, the NMAE under this condition remained below 2%, which is still a low level.

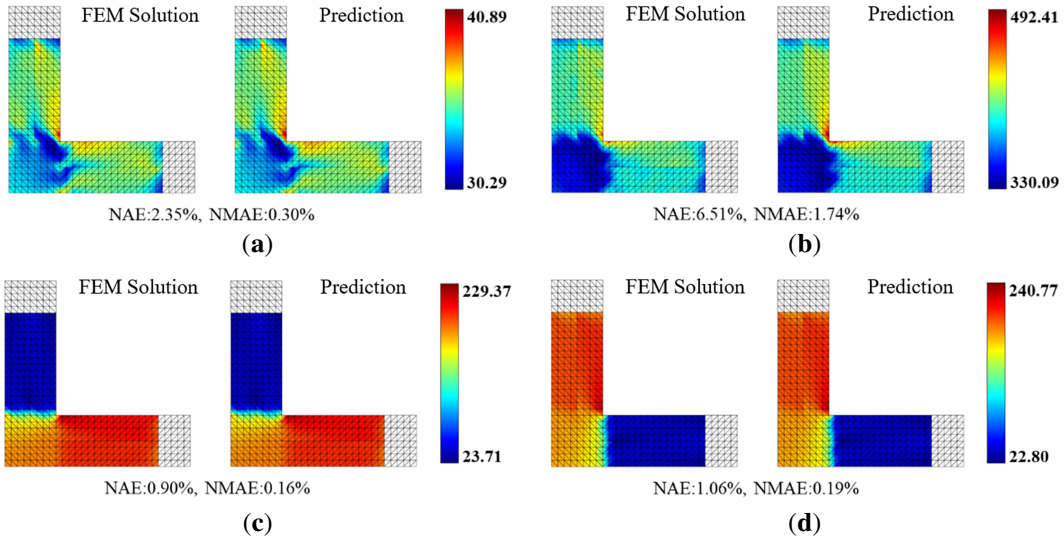


Figure 14: Comparison of membrane surface stress predictions (orthotropic constitutive model, unit: MPa): (**a**) load ratio of 1:1; (**b**) load ratio of 9:9; (**c**) load ratio of 1:5; (**d**) load ratio of 5:1.

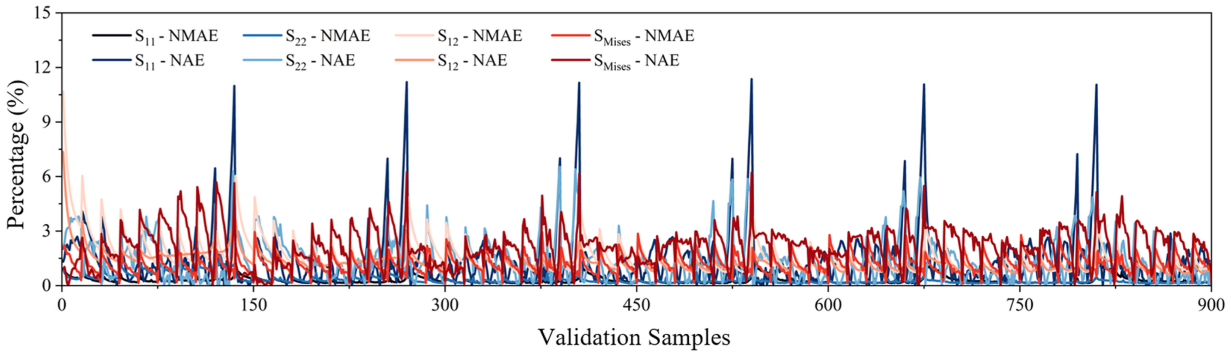


Figure 15: NMAE and NAE curves (orthotropic constitutive model, stress).

Figs. 16 and 17 show the strain field prediction results and the corresponding NMAE and NAE curves for orthotropic membrane materials under different load ratios. The strain contour maps of orthotropic membrane materials predicted by the CAE-ET model under different load ratios were highly consistent with the finite element contour maps. The agreement was observed in the overall distribution pattern, local peak positions, and strain concentration regions. Under the 1:5, 5:1, and 1:1 tensile conditions, the maximum NMAE was 0.99%, and the maximum NAE was 1.27%. This indicates that the model had high-accuracy strain-field prediction ability under both symmetric and asymmetric loading modes. Under the 9:9 tensile condition, the strain peak increased to 0.39, and the local gradient of the strain field became more obvious. The model had greater difficulty capturing such high-gradient local extreme features, causing NAE to increase to 7.45%. However, the NMAE still remained below 1%, and the predicted contour maps maintained good spatial continuity without obvious prediction distortion.

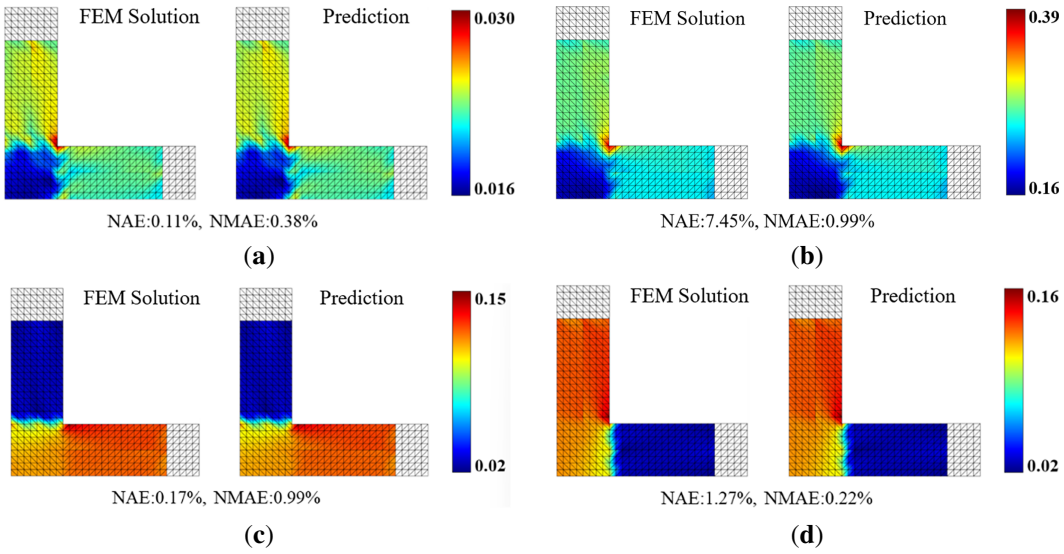


Figure 16: Comparison of membrane surface strain predictions (orthotropic constitutive model): (**a**) load ratio of 1:1; (**b**) load ratio of 9:9; (**c**) load ratio of 1:5; (**d**) load ratio of 5:1.

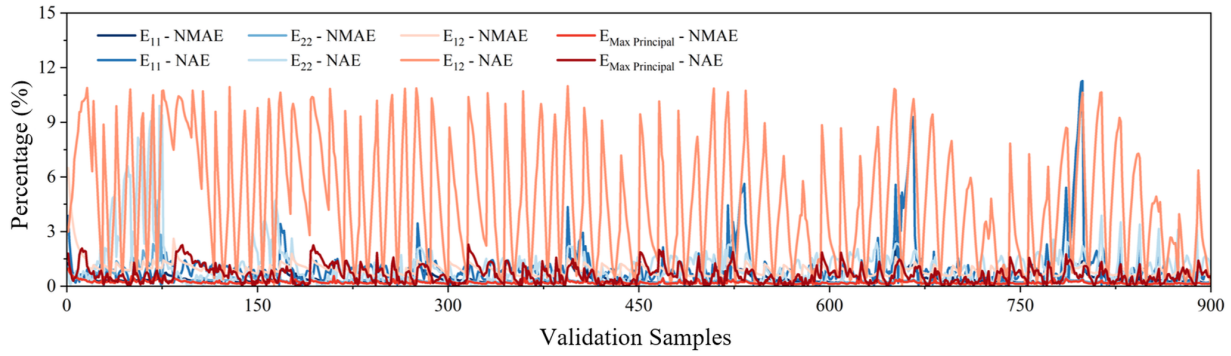


Figure 17: NMAE and NAE curves (orthotropic constitutive model, strain).

Figs. 18–20 show the X- and Y-direction displacement field prediction results and the corresponding NMAE and NAE curves for orthotropic membrane materials under different load ratios. The X- and Y-direction displacement contour maps of orthotropic membrane materials predicted by the CAE-ET model under different load ratios were basically consistent with finite element contour maps. This consistency was reflected in the overall distribution trend, displacement gradient variation, and local displacement features. For the 1:1, 1:5, and 5:1 conditions, the maximum NMAE of X-direction displacement was 2.24%, and the NAE was 2.20%. The maximum NMAE of Y-direction displacement was 1.64%, and the NAE was 0.51%. This indicates that the model reliably predicted both X- and Y-direction displacement components under symmetric and asymmetric loading conditions. Under the 9:9 high-amplitude condition, the peak displacements in the X and Y directions reached 58.30 and 64.94 mm, respectively. The model had greater difficulty capturing such high-gradient displacement features. This led to a certain increase in the NAE values of both displacement components. However, the NMAE still remained within 2.1%, and no obvious shape distortion appeared in the contour maps.

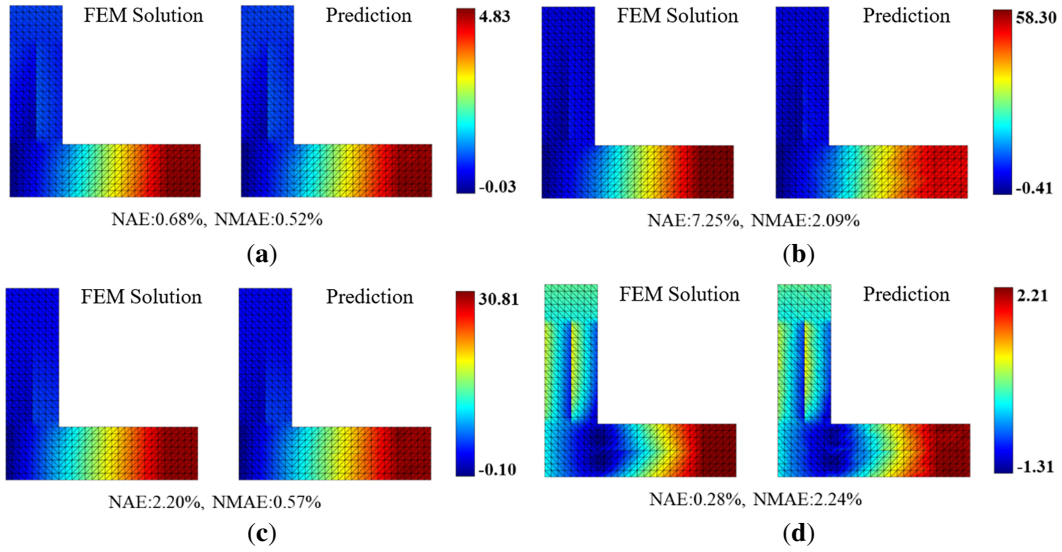


Figure 18: Comparison of membrane surface X-direction displacement predictions (orthotropic constitutive model, unit: mm): (**a**) load ratio of 1:1; (**b**) load ratio of 9:9; (**c**) load ratio of 1:5; (**d**) load ratio of 5:1.

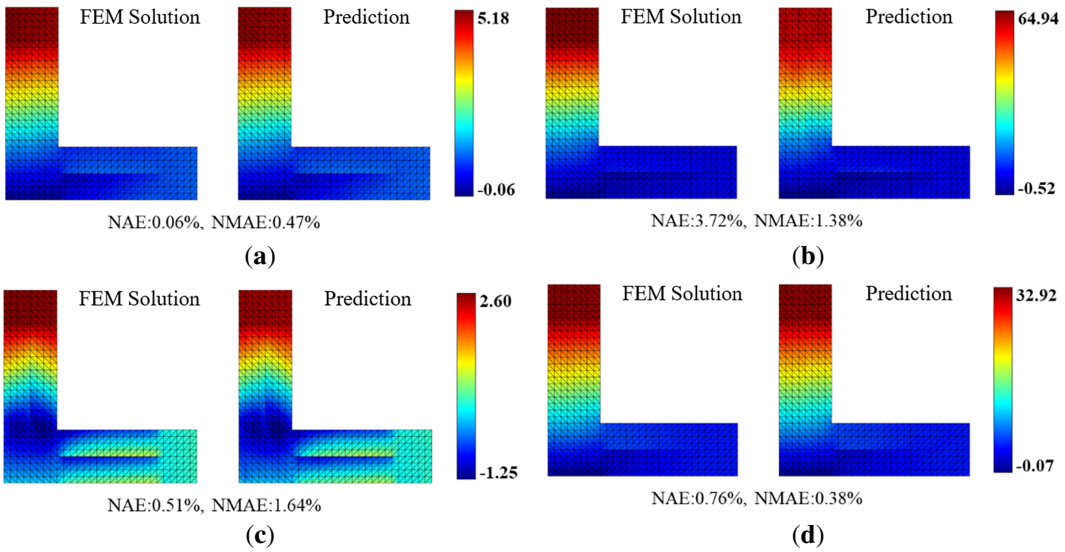


Figure 19: Comparison of membrane surface Y-direction displacement predictions (orthotropic constitutive model, unit: mm): (**a**) load ratio of 1:1; (**b**) load ratio of 9:9; (**c**) load ratio of 1:5; (**d**) load ratio of 5:1.

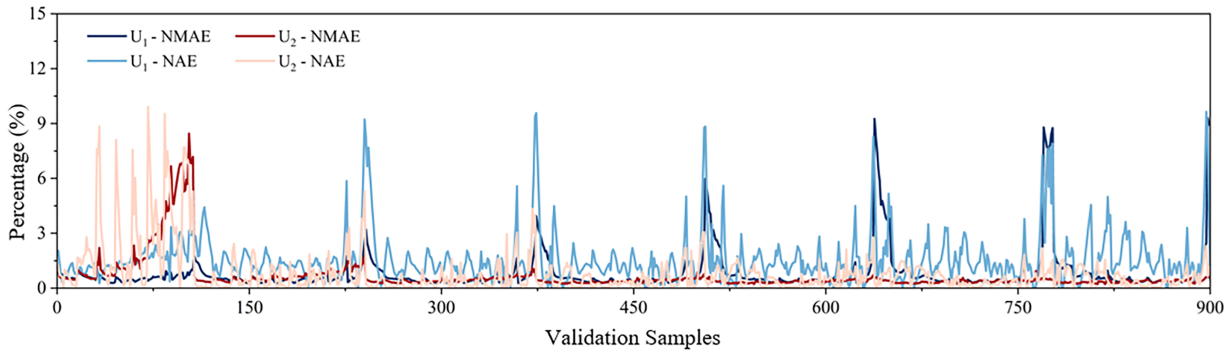


Figure 20: NMAE and NAE curves (orthotropic constitutive model, displacement).

Overall, the stress, strain, and displacement prediction results show that the CAE-ET predictions were generally consistent with the finite element results for orthotropic membrane materials under different load ratios. The model can effectively characterize the full-field mechanical response of membrane materials under plane biaxial tension.

3.4.2 Prediction Performance for Hyperelastic Membrane Materials

In this section, a cross-shaped specimen of hyperelastic membrane material was selected as the validation object. The material parameters are listed in Table 2. Four typical load-ratio conditions were selected: 1:1, 9:9, 1:5, and 5:1. The stress, strain, and displacement fields predicted by the CAE-ET model were validated and compared with corresponding finite element results. The prediction performance of the model under the hyperelastic constitutive condition was evaluated in terms of the stress, strain, and displacement fields.

Figs. 21 and 22 show the stress field prediction results and the corresponding NMAE and NAE curves for hyperelastic membrane materials under different load ratios. The stress contour maps of hyperelastic

membrane materials predicted by the CAE-ET model under different load ratios showed good agreement with finite element contour maps. This agreement was observed in the overall distribution pattern, stress concentration locations, and ranges of high- and low-stress regions. Under the 1:1 and 1:5 tensile conditions, the maximum NMAE was 0.26%, and the maximum NAE was 0.96%. Both values were at low levels. Under the 9:9 and 5:1 tensile conditions, the NAE values increased to 6.86% and 6.27%, respectively. These values were higher than those under the first two conditions, but the NMAE still remained within 1.88%. Under the 5:1 tensile condition, the NAE of stress-field prediction for the hyperelastic membrane material was 6.27%. This was higher than the value of 1.06% for the orthotropic membrane material under the same condition. However, its NMAE was only 0.49%, which remained low. This indicates that the model had high prediction accuracy for the overall spatial distribution of the stress field in hyperelastic membrane materials. The errors were mainly concentrated in local peak regions. Compared with orthotropic membrane materials, local stress responses under the hyperelastic constitutive model showed more obvious nonlinear characteristics. Under asymmetric loading, the stress gradient variation was more complex, increasing the difficulty of capturing peak stress.

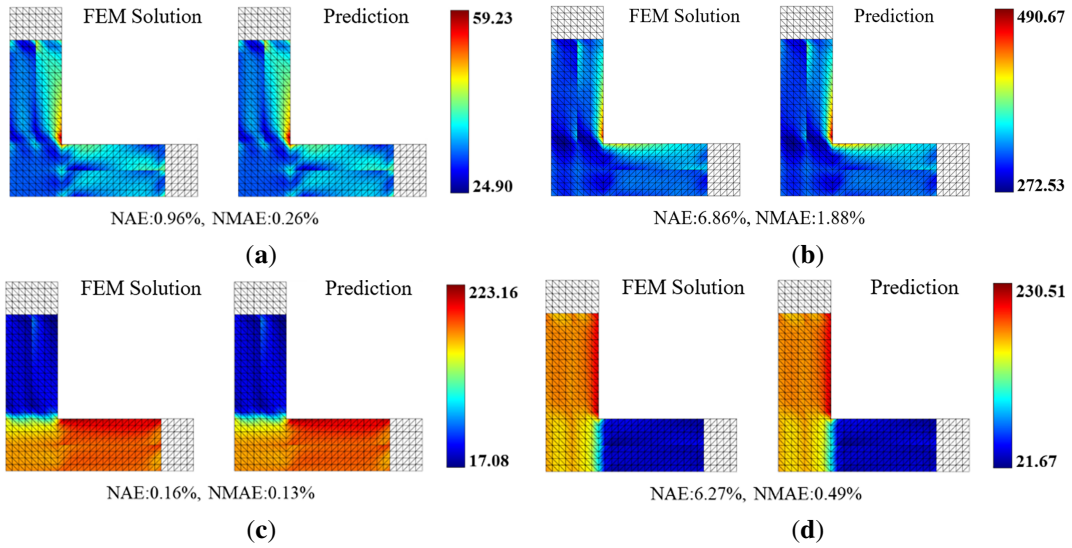


Figure 21: Comparison of membrane surface stress prediction results (hyperelastic constitutive model, unit: MPa): (**a**) load ratio of 1:1; (**b**) load ratio of 9:9; (**c**) load ratio of 1:5; (**d**) load ratio of 5:1.

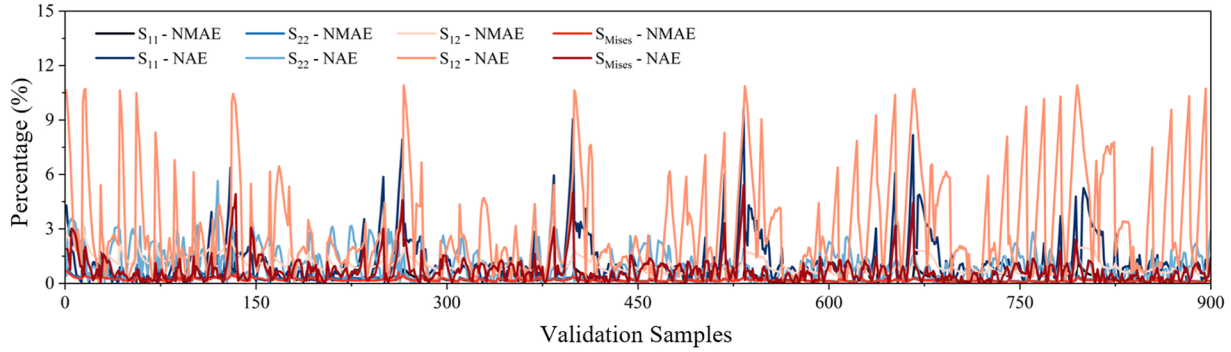


Figure 22: NMAE and NAE curves (hyperelastic constitutive model, stress).

Figs. 23 and 24 show the strain field prediction results and the corresponding NMAE and NAE curves for hyperelastic membrane materials under different load ratios. The strain contour maps of hyperelastic membrane materials predicted by the CAE-ET model under different load ratios showed good agreement with finite element contour maps. This agreement was observed in the overall distribution pattern, local peak positions, and strain concentration regions. Under the 9:9, 1:5, and 5:1 tensile conditions, the maximum NAE was 2.41%, and the maximum NMAE was 1.80%. Both the overall error and peak error were at low levels. Under the 1:1 tensile condition, the NAE was 5.19%, which was higher than those under the other three conditions. However, its NMAE was 1.07%, which was still low. Under the 1:1 tensile condition, the NAE of strain-field prediction for the hyperelastic membrane material was clearly higher than the value of 0.11% for the orthotropic membrane material under the same condition. This is because strain responses under the hyperelastic constitutive model show more obvious nonlinear characteristics than those under the orthotropic model. Under 1:1 loading, local strain concentration and gradient transition were more complex. This increased the difficulty of capturing strain peaks. From the overall NMAE results, the model still maintained good accuracy in predicting the overall distribution of the strain field.

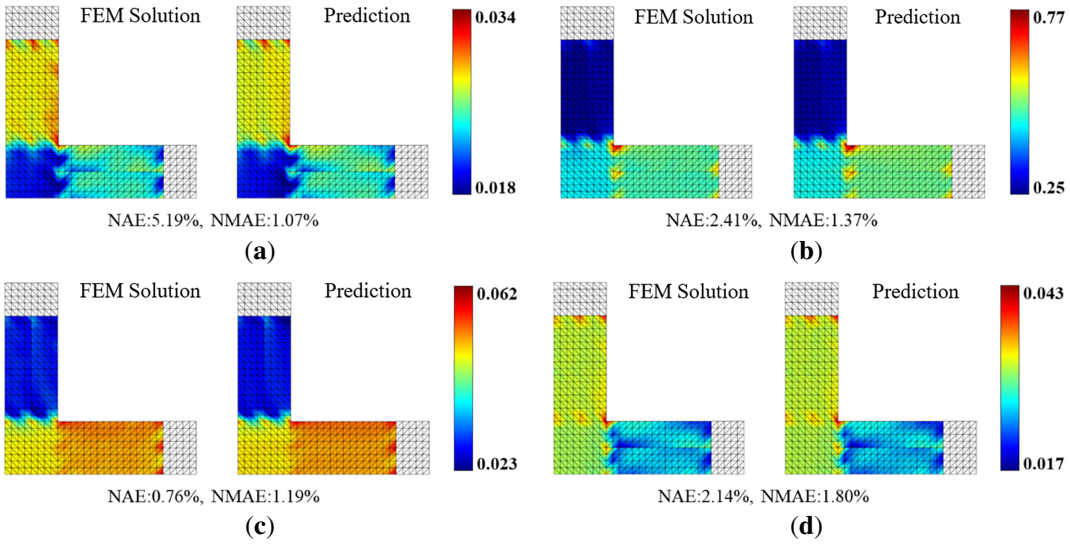


Figure 23: Comparison of membrane surface strain prediction results (hyperelastic constitutive model): (**a**) load ratio of 1:1; (**b**) load ratio of 9:9; (**c**) load ratio of 1:5; (**d**) load ratio of 5:1.

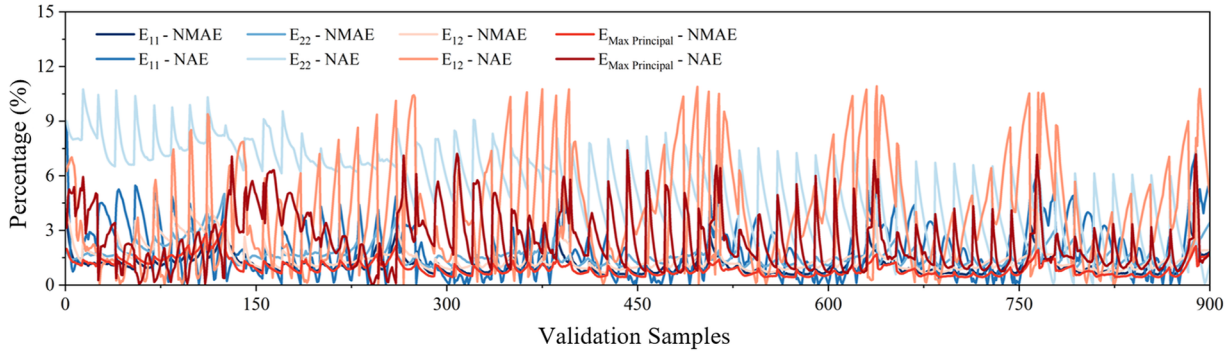


Figure 24: NMAE and NAE curves (hyperelastic constitutive model, strain).

Figs. 25–27 show the X- and Y-direction displacement field prediction results and the corresponding NMAE and NAE curves for hyperelastic membrane materials under different load ratios. The X- and Y-direction displacement contour maps of hyperelastic membrane materials predicted by the CAE-ET model under different load ratios were basically consistent with finite element contour maps. This consistency was reflected in the overall distribution trend, displacement gradient variation, and local displacement features. Under the 1:1 and 1:5 tensile conditions, the overall errors of the X- and Y-direction displacement fields were low, with a maximum NMAE of 0.67%. Under the 1:1 condition, the peak errors in both directions also remained low, with a maximum NAE of 1.34%. However, the NAE of X-direction displacement under the 1:5 condition was 5.77%, which was relatively high. Under the 9:9 and 5:1 tensile conditions, the NAE values of X-direction displacement were 5.51% and 6.04%, respectively. The corresponding NMAE values were 2.74% and 2.22%. The NAE values of Y-direction displacement were 3.42% and 2.11%, respectively. The corresponding NMAE values were 1.56% and 1.98%. The error levels increased compared with the first two conditions, but no obvious shape distortion appeared in the predicted contour maps.

In summary, the CAE-ET model showed good predictive performance for the stress, strain, and displacement fields of hyperelastic membrane materials. Compared with the responses under the orthotropic constitutive model, those under the hyperelastic constitutive model exhibited stronger nonlinear characteristics, resulting in more complex gradients in local peak regions. Consequently, the NAE increased under some conditions. However, the overall NMAE remained low, indicating that the model retained good reconstruction accuracy for the overall distribution of the full-field responses.

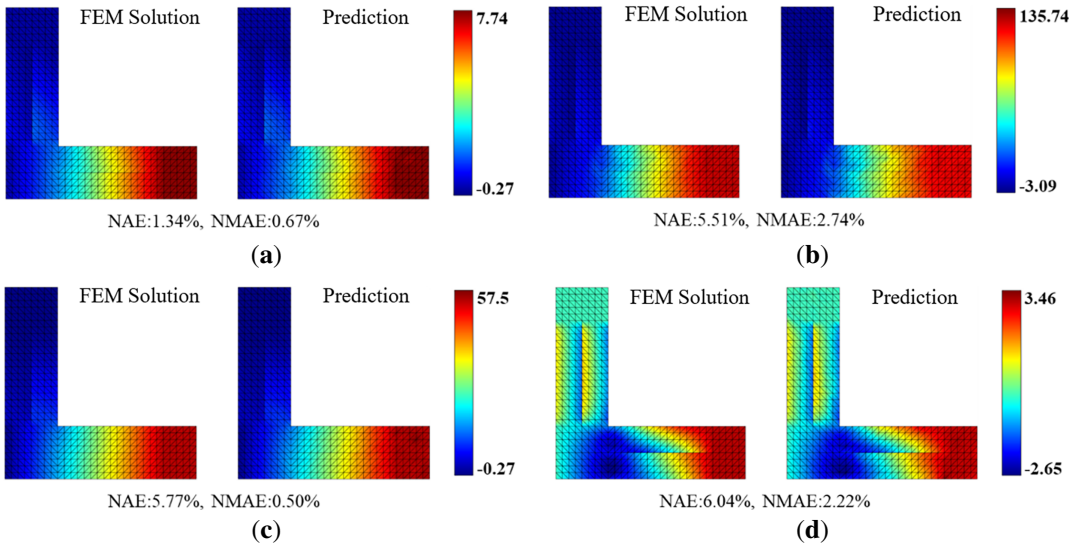


Figure 25: Comparison of membrane surface X-direction displacement prediction results (hyperelastic constitutive model, unit: mm): (**a**) load ratio of 1:1; (**b**) load ratio of 9:9; (**c**) load ratio of 1:5; (**d**) load ratio of 5:1.

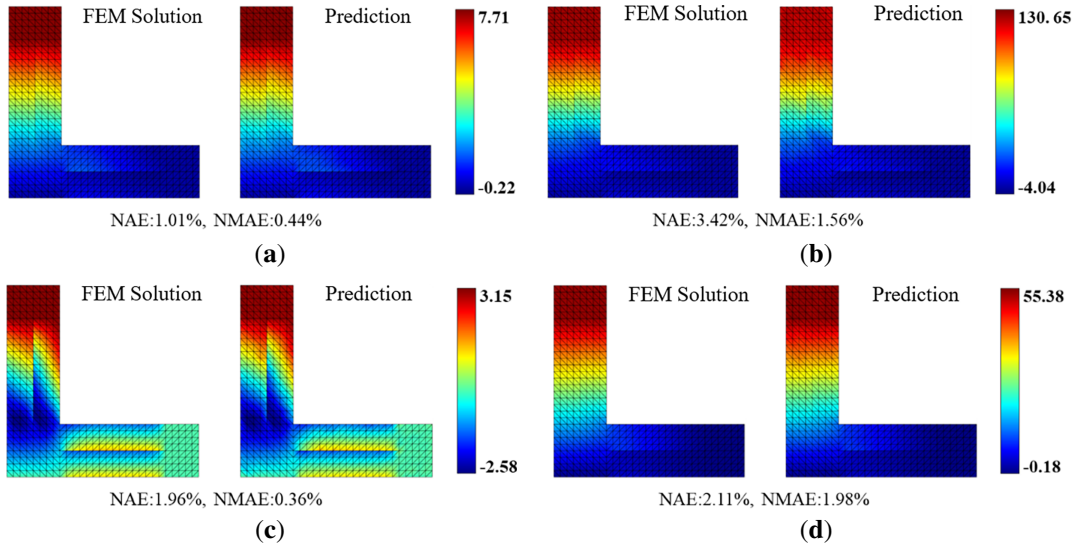


Figure 26: Comparison of membrane surface *Y*-direction displacement prediction results (hyperelastic constitutive model, unit: mm): (**a**) load ratio of 1:1; (**b**) load ratio of 9:9; (**c**) load ratio of 1:5; (**d**) load ratio of 5:1.

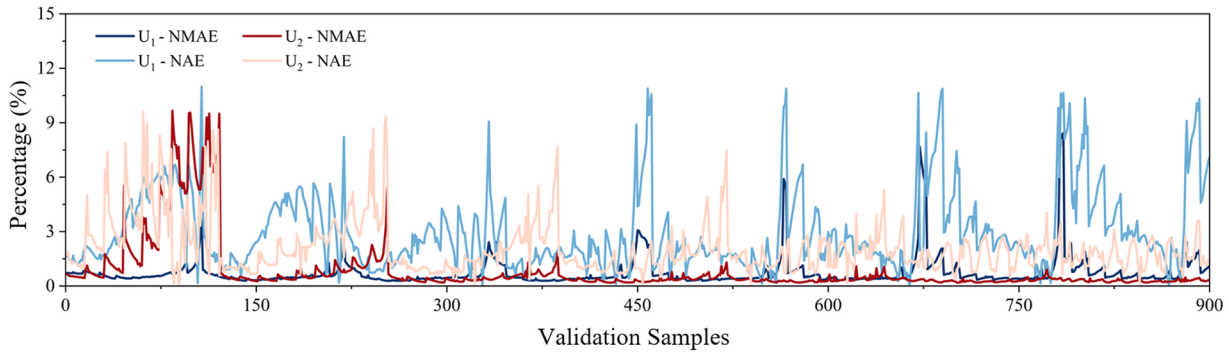


Figure 27: NMAE and NAE curves (hyperelastic constitutive model, displacement).

The latent-code regression results on the test set and the full-field response prediction results show that, under the current dataset size, the CAE-ET model can effectively reconstruct the overall spatial distributions of the stress, strain, and displacement fields under different biaxial loading conditions. It can also identify the main response regions, local concentration regions, and peak positions. In the present results, relatively large peak errors mainly occurred under high-load or asymmetric loading conditions and in regions with large local gradients. This indicates that local peak prediction is more sensitive to the sample coverage of the corresponding loading and response conditions. Increasing the number of representative samples under high-load conditions and in strongly nonlinear and high-gradient response regions may further improve the prediction accuracy of local peak values. Expanding the coverage of material parameters, biaxial load combinations, loading stages, and complex mechanical conditions may also improve the prediction accuracy and generalization performance of the model. It should also be noted that both the training data and the samples used for independent prediction validation were generated using the same finite element modeling framework. Therefore, the current validation mainly reflects the prediction accuracy of the CAE-ET model relative to the finite element results within the current dataset. The results cannot be directly extended to new membrane materials, specimen geometries, boundary conditions, or loading conditions outside the training

range. Before application to new materials or engineering conditions, a new dataset should be constructed, and targeted validation should be conducted through experiments or further finite element analyses.

3.5 Computational Efficiency Evaluation of the CAE-ET Model

To quantitatively evaluate the computational efficiency of the CAE-ET model, model training was completed based on the PyTorch framework on an NVIDIA GTX 1080 GPU hardware platform. Six typical load-ratio conditions were then tested in the same computing environment and compared with the traditional finite element method (FEM) in terms of computation time.

Fig. 28 shows the computational time of the CAE-ET model and the finite element method under different load ratios. The results showed that, after CAE-ET model training was completed, a single stress-field prediction took about 0.35 s, with fluctuations within 0.02 s. In contrast, the traditional finite element method took about 32.3–35.5 s under the same conditions. The computational efficiency improved by about 90–100 times. Repeated tests under different load-ratio conditions showed that the prediction time fluctuation of CAE-ET was clearly smaller than that of the finite element method. This efficiency advantage mainly comes from the rapid inference process after CAE-ET model training. Only ET prediction of low-dimensional feature codes and CAE decoder reconstruction of the mechanical field response are required. This avoids repeated nonlinear iterative solution in the traditional finite element method for each new condition. Therefore, the model is suitable for rapid multi-condition evaluation and auxiliary analysis in structural online monitoring.

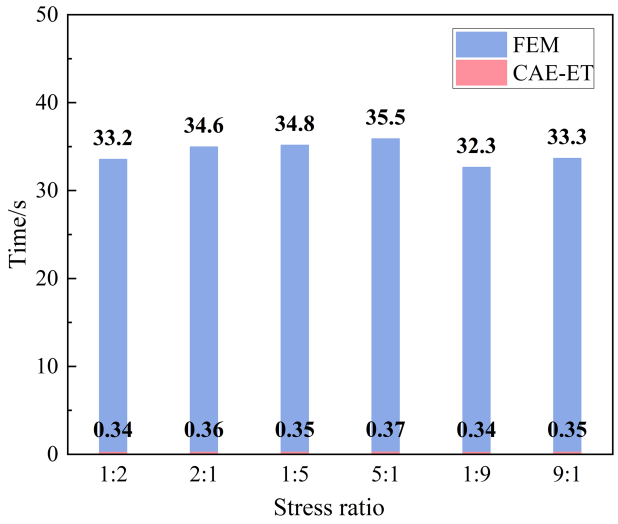


Figure 28: Comparison of computation times between the CAE-ET model and finite element analysis.

4 Conclusions

This study proposes a CAE-ET rapid prediction model that integrates a convolutional autoencoder and extremely randomized trees. The model is developed for rapid prediction of the full-field mechanical response of membrane materials under biaxial tension. The main conclusions are as follows.

(1) Compared with existing studies, this study further compared different regression models for mapping the input parameters to the low-dimensional latent codes of the CAE. The five-fold cross-validation results show that ET achieved higher and less fluctuating R^2 values than DNN and LSTM. It also has lower MAE and MSE. These results indicate that ET is more suitable for the low-dimensional code

regression task under the limited-sample conditions in this study. The resulting CAE-ET model can effectively extract low-dimensional features from the mechanical fields of membrane materials and establish a stable mapping between the input parameters and latent codes. It also demonstrates high prediction accuracy and good stability for the full-field mechanical responses of membrane materials under biaxial tension.

(2) The CAE-ET model can predict the full-field mechanical responses of membrane materials under different load ratios with good accuracy. The predicted results are generally consistent with the finite element results in terms of the overall distribution patterns and main response regions. In most cases, the NMAE was below 2%, and the NAE was generally within 10%. These results indicate that the model has good full-field response reconstruction capability. However, its ability to capture local extreme-value features still requires further improvement. Increasing the number of effective samples under high-load conditions and in strongly nonlinear and high-gradient response regions may further improve the prediction accuracy of local peak values.

(3) A single prediction of the CAE-ET model took about 0.34–0.37 s. Compared with the traditional finite element method, which takes 32.3–35.5 s, the efficiency improves by about 90–100 times. The prediction time fluctuation was also small. This model can rapidly and stably predict the full-field mechanical responses of membrane materials with different constitutive descriptions under biaxial tension. It provides an effective method for efficient characterization of membrane mechanical behavior and evaluation of mechanical performance.

The proposed CAE-ET model demonstrated high prediction accuracy and computational efficiency within the scope of this study. However, the current comparison covered only a limited range of regression models. Future work will expand the range of membrane materials and loading conditions and investigate additional advanced machine-learning methods to further improve the generalization capability and engineering applicability of the model.

Acknowledgement: The authors thank the State Key Laboratory of Intelligent Construction and Healthy Operation and Maintenance of Deep Underground Engineering for providing experimental assistance. The help from the laboratory staff and students during the tests is also greatly appreciated.

Funding Statement: This work was supported by The National Natural Science Foundation of China (No. 52278229, No. 52308222).

Author Contributions: The authors confirm contribution to the paper as follows: conceptualization, Jinpeng Zuo; methodology, Jinpeng Zuo; formal analysis, Jinpeng Zuo and Shuhuan Fei; investigation, Jinpeng Zuo; resources, Yingying Zhang; data curation, Shuhuan Fei; writing—original draft preparation, Jinpeng Zuo; writing—review and editing, Yingying Zhang, Shuhuan Fei, Junhao Xu and Yushuai Zhao; supervision, Yushuai Zhao; project administration, Yingying Zhang and Junhao Xu; funding acquisition, Yingying Zhang. All authors reviewed and approved the final version of the manuscript.

Availability of Data and Materials: The data that support the findings of this study are available from the corresponding author upon reasonable request.

Ethics Approval: Not applicable.

Conflicts of Interest: The authors declare no conflicts of interest.

References

1. Xu J, Zhang Y, Yu Q, Zhang L. Analysis and design of fabric membrane structures: a systematic review on material and structural performance. Thin Walled Struct. 2022;170(5):108619. doi:10.1016/j.tws.2021.108619.
2. Ambroziak A. Mechanical properties of Precontraint 1202S coated fabric under biaxial tensile test with different load ratios. Constr Build Mater. 2015;80(8):210–24. doi:10.1016/j.conbuildmat.2015.01.074.
3. Shi T, Hu J, Chen W, Gao C. Biaxial tensile behavior and strength of architectural fabric membranes. Polym Test. 2020;82:106230. doi:10.1016/j.polymertesting.2019.106230.
4. Zhang Y, Xu J, Zhang Q. Advances in mechanical properties of coated fabrics in civil engineering. J Ind Text. 2018;48(1):255–71. doi:10.1177/1528083716679159.
5. Hild F, Roux S. Digital image correlation: from displacement measurement to identification of elastic properties—a review. Strain. 2006;42(2):69–80. doi:10.1111/j.1475-1305.2006.00258.x.
6. Avril S, Bonnet M, Bretelle AS, Grédiac M, Hild F, Ienny P, et al. Overview of identification methods of mechanical parameters based on full-field measurements. Exp Mech. 2008;48(4):381–402. doi:10.1007/s11340-008-9148-y.
7. Grédiac M, Pierron F, Avril S, Toussaint E. The virtual fields method for extracting constitutive parameters from full-field measurements: a review. Strain. 2006;42(4):233–53. doi:10.1111/j.1475-1305.2006.tb01504.x.
8. Pargana JB, Lloyd-Smith D, Izzuddin BA. Advanced material model for coated fabrics used in tensioned fabric structures. Eng Struct. 2007;29(7):1323–36. doi:10.1016/j.engstruct.2006.09.001.
9. Minami H. A multi-step linear approximation method for nonlinear analysis of stress and deformation of coated plain-weave fabric. J Text Eng. 2006;52(5):189–95. doi:10.4188/jte.52.189.
10. Galliot C, Luchsinger RH. A simple model describing the non-linear biaxial tensile behaviour of PVC-coated polyester fabrics for use in finite element analysis. Compos Struct. 2009;90(4):438–47. doi:10.1016/j.compstruct.2009.04.016.
11. Chen SH, Yu HQ, Guo Z, Null RF, Qi DP. The FEM-prediction on tensile performance of woven membrane materials under uni and bi-axial loads. J Fiber Bioeng Inform. 2024;3(4):244–9. doi:10.3993/jfbi03201109.
12. Jekel CF, Venter G, Venter MP. Modeling PVC-coated polyester as a hypoelastic non-linear orthotropic material. Compos Struct. 2017;161(6):51–64. doi:10.1016/j.compstruct.2016.11.019.
13. Yang B, Yu Z, Zhang Q, Shang Y, Yan Y. The nonlinear orthotropic material model describing biaxial tensile behavior of PVC coated fabrics. Compos Struct. 2020;236(4):111850. doi:10.1016/j.compstruct.2019.111850.
14. Gao C, Chen W, Hu J, Zhao B. A new constitutive model on biaxial tensile behavior of architectural fabrics. Polym Test. 2020;87:106519. doi:10.1016/j.polymertesting.2020.106519.
15. Zhang L, Zhang Y, Song W, Xu J, Xue J. A nonlinear damage constitutive model of PVC coated fabrics. Structures. 2021;30(1):368–77. doi:10.1016/j.istruc.2021.01.027.
16. Sun C, Zhang L, Li C. A high efficient constitutive model of coated plain-weave fabrics under uniaxial tensile loads in arbitrary directions. J Ind Text. 2022;52(2):1–20. doi:10.1177/15280837221137013.
17. Pang Y, Qiu G, Gong J. A material model describing the nonlinear biaxial tensile behavior of fabric membrane in precise forming for inflated structures. Structures. 2024;70:107884. doi:10.1016/j.istruc.2024.107884.
18. Liang L, Liu M, Martin C, Sun W. A deep learning approach to estimate stress distribution: a fast and accurate surrogate of finite-element analysis. J R Soc Interface. 2018;15(138):20170844. doi:10.1098/rsif.2017.0844.
19. Jiang H, Nie Z, Yeo R, Farimani AB, Kara LB. StressGAN: a generative deep learning model for two-dimensional stress distribution prediction. J Appl Mech. 2021;88(5):051005. doi:10.1115/1.4049805.
20. Hoq E, Aljarrah O, Li J, Bi J, Heryudono A, Huang W. Data-driven methods for stress field predictions in random heterogeneous materials. Eng Appl Artif Intell. 2023;123(4):106267. doi:10.1016/j.engappai.2023.106267.
21. Yang Z, Yu CH, Buehler MJ. Deep learning model to predict complex stress and strain fields in hierarchical composites. Sci Adv. 2021;7(15):eabd7416. doi:10.1126/sciadv.abd7416.
22. Bhaduri A, Gupta A, Graham-Brady L. Stress field prediction in fiber-reinforced composite materials using a deep learning approach. Compos Part B Eng. 2022;238(11):109879. doi:10.1016/j.compositesb.2022.109879.
23. Mohammadzadeh S, Lejeune E. Predicting mechanically driven full-field quantities of interest with deep learning-based metamodels. Extrem Mech Lett. 2022;50(5):101566. doi:10.1016/j.eml.2021.101566.

24. Maurizi M, Gao C, Berto F. Predicting stress, strain and deformation fields in materials and structures with graph neural networks. Sci Rep. 2022;12(1):21834. doi:10.1038/s41598-022-26424-3.
25. Rashid MM, Pittie T, Chakraborty S, Krishnan NMA. Learning the stress-strain fields in digital composites using Fourier neural operator. iScience. 2022;25(11):105452. doi:10.1016/j.isci.2022.105452.
26. Deshpande S, Rappel H, Hobbs M, Bordas SPA, Lengiewicz J. Gaussian process regression + deep neural network autoencoder for probabilistic surrogate modeling in nonlinear mechanics of solids. Comput Meth Appl Mech Eng. 2025;437(6):117790. doi:10.1016/j.cma.2025.117790.
27. Xu J, Sheng L, Zhang Y, Fei S, Zhao Z. A novel end-to-end deep learning model for predicting the full stress field of tensioned membrane structures. KSCE J Civ Eng. 2025;29(4):100073. doi:10.1016/j.kscej.2024.100073.
28. Xu JH, Zhang YY, Zhao YS, Fei SH, Chen PJ, Zhou Y. A hyperelastic constitutive model for architectural PTFE-coated fabric under biaxial tension. Eng Mech. 2025;42(9):220–32. (In Chinese). doi:10.6052/j.issn.1000-4750.2023.05.0340.
29. Goodfellow I, Bengio Y, Courville A. Deep learning. Cambridge, MA, USA: MIT Press; 2016.
30. Nair V, Hinton GE. Rectified linear units improve restricted Boltzmann machines. In: Proceedings of the 27th International Conference on Machine Learning; 2010 Jun 21–24; Madison, WI, USA. p. 807–14.
31. Wang Z, Bovik AC, Sheikh HR, Simoncelli EP. Image quality assessment: from error visibility to structural similarity. IEEE Trans Image Process. 2004;13(4):600–12. doi:10.1109/tip.2003.819861.